University of Michigan, Ann Arbor

Undergraduate Thesis

A Probe into Propagators

Author:
Jiani FEI

Supervisor:
Dr. Emanuel GULL

An honors thesis submitted for Bachelor of Science degree

in the

Gull Group
Physics Department

May 2, 2021

Abstract

by Jiani FEI

Quantum field theory (QFT) is interesting in the sense that it explains the subatomic world with a mathematical framework that is both essential and beautiful. Equations in quantum field theory are well understood while very difficult to solve. Due to the imaginary nature of the partition function, field theory under finite temperature (thermal QFT) employs the Matsubara formalism majorly in practice, which 'Wick' rotates the Euclidean time by 90 degrees in the complex plane (multiply by 'i') and evolves in this 'imaginary time' [1].

Matsubara formalism involves the propagators (Green's functions) that corresponds to the spectral functions measurable in experiments, though in 'real time'. Physics lying beneath different spectral functions is a heated area of research, which for instance provides evidence for the exciting high-Tc superconductivity phenomena. However, one big obstacle there, between theories and experiments, is the abstruse relation between the imaginary- and real-time formalism, or their corresponding (Fourier transformed) frequency components. The kernel relating 'imaginary' with 'real' domain propagators is notoriously ill-conditioned.

Finding an operational procedure that takes in Matsubara Green's function data and outputs real-frequency data is therefore of enormous need as the post-processing of quantum simulations. Analytic continuation, by the uniqueness theorem, can extend analytic functions uniquely into a bigger domain. It is used in practice as the algorithm for this transformation. Existing methods such as Maximum Entropy (MaxEnt) method and Padé continued fraction fit involve instabilities that brings unphysical features or resolution ambiguity. Like although Padé is cool enough, it still would get the poles in the wrong half of the complex plane and would not get the correct normalization in general.

This thesis will majorly (Chapter 1 and Chapter 2) develop methods to replace MaxEnt and Padé, namely the Nevanlinna method. Nevanlinna (and Carathéodory) continuation method is based on interesting mathematics and enforce the causal analytic structure on the Green's function (both single-particle and matrix-valued ones). It has shown unprecedented accuracy in some application examples. The resulting paper have been published in *Physical Review Letters* (Phys. Rev. Lett. 126, 056402) as the Editors' Suggestion.

Chapter 3 is a real-material simulation that I finished with the guidance of Dr. Chia-Nan Yeh. I have used the self-energy embedding theory (SEET) and the code developed by our group to simulate the spectral function of the strontium titanate ($SrTiO_3$). This was a fruitful learning experience of mine where I have appreciated the beautiful math in numerical algorithms, probing more into the propagator (response function) physics, as well as seeing how condensed matter simulations talk to experiments in practice.

Acknowledgement

I would especially love to thank prof. Emanuel Gull for his care and help during my stay at his group. I had little experience in research when I came to his group, but he was always willing to answer my questions in great detail and patience. The many discussions with him are always enjoyable. His dedication and professionalism towards his work has also inspired me a great lot.

I am also much grateful for Dr. Chia-Nan Yeh and Dr. Sergei Iskakov for their guidance. Chia-Nan has unconditionally provided me with his notes and code to study during my SEET study. Together with Sergei, they had answered my bunches of questions. Very much thanks towards them. All other group members at the Gull group, Xinyang, Jia, Runxue, etc. are very nice people who I love to work and talk with. It is all of you that made my experience here extremely worthy!

At last, I want to thank my parents for their great love and support as always. They have encouraged me to do things that I feel passionate for. I have grown up happily largely because of them! Best regards to all of the people that I just mentioned. :)

Contents

Chapter 1

Nevanlinna Analytic Continuation

The main result of this chapter have been published in *Physical Review Letters* as "Nevanlinna Analytic Continuation (Jiani Fei, Chia-Nan Yeh, and Emanuel Gull)" (Phys. Rev. Lett. 126, 056402; Editors' Suggestion).

1.1 Relationship between Nevanlinna function and Green's Function

In the field of complex analysis, a Nevanlinna function is a complex function which is an analytic function on the open upper half-plane $\mathcal{C}^+$ and has non-negative imaginary part, i.e. maps into $\overline{\mathcal{C}^+}$ (the overline denotes inclusion of the boundary) [2]. Denote the class of Nevanlinna functions as N.

The retarded Green's function G^R is analytic in the upper half of the complex plane, $\mathcal{C}^+$, and contains singularities in the lower half plane. The Matsubara Green's function $\mathcal{G}(i\omega_n)$ and the retarded Green's function $G^R(\omega + i\eta)$ can be expressed consistently by replacing the variables $i\omega$ and $\omega + i\eta$ with a single complex variable z. Analytic continuation is used to obtain G^R from $\mathcal{G}$.

We state that the negative of the Green's function $\mathcal{G}$ restricted to $\mathcal{C}^+$ (involving $\mathcal{G}(i\omega_n)$ with $\omega_n > 0$ and $G^R(\omega + i\eta)$ with $\eta > 0$) is a Nevanlinna function. This is to say, denoting $\mathcal{N}\mathcal{G} = -\mathcal{G}$, then $\mathcal{N}\mathcal{G} : \mathcal{C}^+ \to \overline{\mathcal{C}^+}$ and $\mathcal{N}\mathcal{G} \in$ N.

Proof. Green's function restricted to $\mathcal{C}^+$ can be formulated by Lehmann representation as,

$$\mathcal{G}(\gamma, z) = \frac{1}{Z} \sum_{m,n} \frac{|\langle m|c_\gamma^\dagger|n\rangle|^2}{z + E_n - E_m}(e^{-\beta E_n} + e^{-\beta E_m}) \tag{1.1}$$

where E_m and E_n are eigenvalues corresponding to eigenstates $|m\rangle$ and $|n\rangle$ of a given Hamiltonian system, Z is the partition function, β is the inverse temperature, $c_\gamma^\dagger$ is the creation operator for orbital γ.

Now we prove any summand on the r.h.s. of (2.12) belongs to the Nevanlinna function class N. Denote and notice that,

$$A = \frac{1}{Z}|\langle m|c_\gamma^\dagger|n\rangle|^2(e^{-\beta E_n} + e^{-\beta E_m}) \geqslant 0 \tag{1.2}$$

Let $z = x + yi$ where $y > 0$, i.e. $z \in \mathcal{C}^+$. Then each summand can be represented as,

$$S = \frac{A}{x + E_n - E_m + yi} = \frac{A(x + E_n - E_m - yi)}{(x + E_n - E_m)^2 + y^2} \tag{1.3}$$

$$Im\{S\} = -\frac{Ay}{(x + E_n - E_m)^2 + y^2} \leqslant 0 \tag{1.4}$$

Due to the closure relation of Nevanlinna function class, summing all summands in (2.12) gives $Im\{\mathcal{G}(\gamma, z)\} \leqslant 0$ and thus $Im\{\mathcal{NG}(\gamma, z)\} \geqslant 0$ for $z \in \mathcal{C}^+$. And since $\mathcal{NG}$ is obviously analytic in the upper half plane with poles on the real axis, it belongs to the Nevanlinna function class $\mathbb{N}$. □

1.2 Schur Algorithm
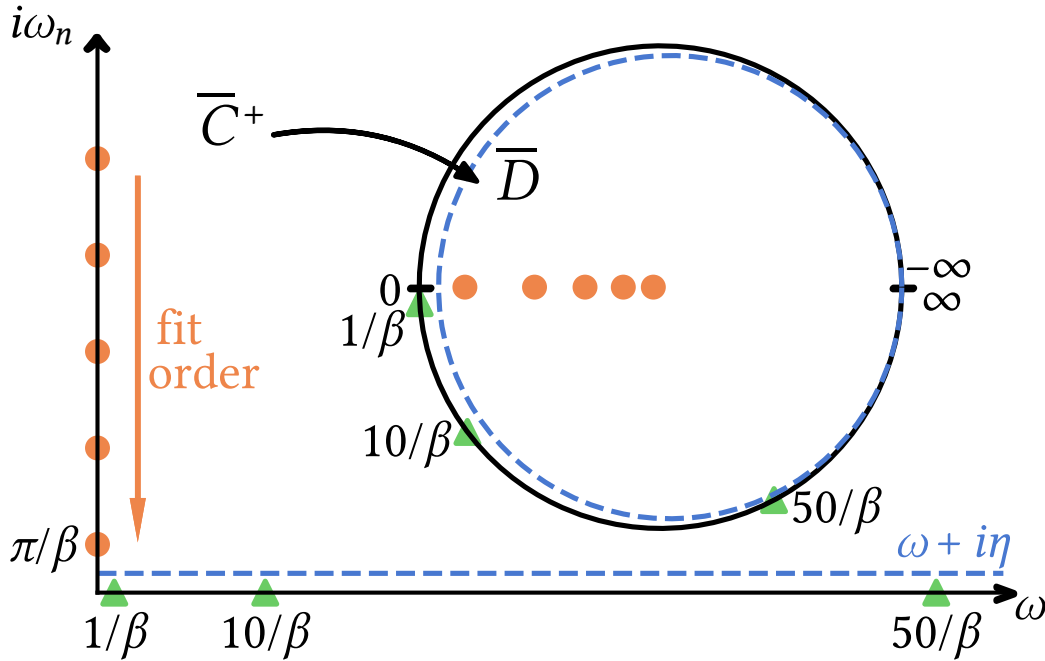

Figure 1.1: Analytic continuation setup with fermion Matsubara points at $i\omega_n$ and real frequency axis ω. The retarded Green's function is evaluated η (small) above the real axis. Inset: Möbius transform of the closed upper half plane $\overline{\mathcal{C}^+}$ to the closed unit disk $\overline{\mathcal{D}}$.

To perform analytic continuation from the Matsubara to the real axis, we aim to find an interpolant for $\mathcal{NG} = -\mathcal{G}$ in the class of Nevanlinna functions $\mathbb{N}$, rather than a generic continued fraction. By construction, this function will pass through all Matsubara points (see Fig. 1.1) and have a positive imaginary part in the upper half plane, including just above the real axis. Spectral functions $A(\omega) = \lim_{\eta \to 0^+} \frac{1}{\pi} Im\{\mathcal{NG}(\omega + i\eta)\}$ are therefore intrinsically positive, avoiding the common failure of Padé interpolants.

After obtaining a set of positive Matsubara frequency Green's function data and negate them, we have a set of functions,

$$f(Y_i) = C_i \quad i = 1, 2, \ldots, M \tag{1.5}$$

where $Y_i = i\omega_n \in \mathcal{C}^+$ and $C_i \in \mathcal{C}^+$. We look for the class of Nevanlinna functions $\{f(z)\}$ so that (1.5) exists. Such f are interpolants to $\mathcal{NG}$.

We use the modified Schur algorithm to interpolate the Nevanlinna function needed [3]. Schur studied a class (Schur class S) of holomorphic disk functions mapping from $\mathcal{D}$ to $\overline{\mathcal{D}}$, where $\mathcal{D} = \{z : |z| < 1\}$ is the open unit disk in the complex plane, $\overline{D}$ the closed unit disk. Schur found every Schur function has a continued fraction expansion where the parameters can be recursively defined. With this expansion formula, Nevanlinna later developed an iterative algorithm to interpolate Schur functions [2]. Schur algorithm was modified to expand all contractive functions [4], which are holomorphic functions mapping from $\mathcal{C}^+$ to $\overline{\mathcal{D}}$. Denote contractive function class as B. The invertible Möbius transform $h : \overline{\mathcal{C}^+} \to \overline{\mathcal{D}}, z \mapsto \frac{z-i}{z+i}$ on function value (with half-plane domain unchanged) maps Nevanlinna functions one-to-one to contractive functions (see Fig. 1.1). The Nevanlinna interpolation problem is therefore mapped into the problem of constructing the contractive function θ which is Möbius transformed from $\mathcal{NG}$,

$$\theta(Y_i) = \lambda_i = h(C_i) = \frac{C_i - i}{C_i + i} \quad i = 1, 2, \ldots, M \tag{1.6}$$

where Y_i is the i-th Matsubara frequency, C_i is the value of $\mathcal{NG}$ at Y_i, and λ_i is the value of θ at Y_i. See the below diagram for function mappings.

f : Nevanlinna function $\in$ N
g : Schur function $\in$ S
θ : Contractive function $\in$ B
h/h_1 : Conformal mapping (e.g. Möbius transform)
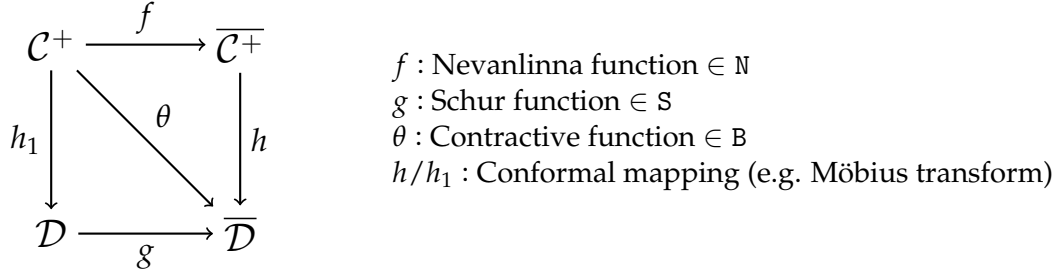
The modified Schur algorithm is an iterative method which decreases the number of interpolation nodes by 1 in each step. The first step of reduction is shown below [4],

$\theta \in$ B satisfies the condition,

$$\theta(Y_1) = \lambda_1 \quad |\lambda_1| < 1 \tag{1.7}$$

if and only if it admits the representation,

$$\theta(z) = \frac{\phi(z) + \lambda_1}{\lambda_1^* \phi(z) + 1} \tag{1.8}$$

where $\phi \in$ B and $\phi(Y_1) = 0$. Since $Y_1 \in \mathcal{C}^+$, $\phi(z)$ admits the representation,

$$\phi(z) = \frac{z - Y_1}{z - Y_1^*} \theta_1(z) \tag{1.9}$$

where θ_1 is an arbitrary function such that $\theta_1 \in$ B.

Proof. We use the conformal mapping $h_1(z) = \frac{z - Y_1}{z - Y_1^*}$ to establish the one-to-one correspondence of θ to a Schur function g. Then,

$$g(0) = \theta(h_1^{-1}(0)) = \theta(Y_1) = \lambda_1 \tag{1.10}$$

Schur defines λ_1 to be a parameter inside his expansion formula and g_1 to be the recursively defined next Schur function if $g(0) = \lambda_1$ as [3],

$$xg_1(x) = \frac{g(x) - \lambda_1}{1 - \lambda_1^* g(x)} \tag{1.11}$$

where $x \in \mathcal{D}$.

We let $\theta_1(z) = g_1(h_1(z))$, then it is ensured that $\theta_1(z) \in B$. Equation (1.11) can be rewritten as,

$$x\theta_1(h_1^{-1}(x)) = \frac{\theta(h_1^{-1}(x)) - \lambda_1}{1 - \lambda_1^* \theta(h_1^{-1}(x))} = \phi(h_1^{-1}(x)) \tag{1.12}$$

Thus, firstly,

$$\phi(z) = \frac{\theta(z) - \lambda_1}{1 - \lambda_1^* \theta(z)} \tag{1.13}$$

$$\theta(z) = \frac{\phi(z) + \lambda_1}{\lambda_1^* \phi(z) + 1} \tag{1.14}$$

where $z \in \mathcal{C}^+$. Secondly,

$$\phi(h_1^{-1}(x)) = h_1(h_1^{-1}(x))\theta_1(h_1^{-1}(x)) \tag{1.15}$$

$$\phi(z) = h_1(z)\theta_1(z) = \frac{z - Y_1}{z - Y_1^*}\theta_1(z) \tag{1.16}$$

where $z \in \mathcal{C}^+$, $\phi = h_1\theta_1 \in B$ and $\phi(Y_1) = 0$. □

Then a $\theta \in B$ interpolation with M nodes reduces to a $\theta_1 \in B$ interpolation with M-1 nodes. We get the interpolation node values $\theta_1(Y_j)$ for $j = 2, 3, \ldots, M$ by equations (1.8) and (1.9). Each reduction releases 1 node constraint. Therefore, after M steps of reduction, we get an arbitrary contractive function $\theta_M(z) \in B$ and the continued fraction expansion form $\theta[z; \theta_M(z)]$.

The substitution procedure can be written in a more compact matrix form. Denote the intermediate contractive function after k steps of reduction as θ_k, $\lambda_1^{(0)} = \lambda_1 = \theta(Y_1)$, $\lambda_{k+1}^{(k)} = \theta_k(Y_{k+1})$ ($k = 1, 2, \ldots, M - 1$), $\theta_M(z) \in B$. Then we have the central equations,

$$\theta(z) = \frac{a_k(z)\theta_k(z) + b_k(z)}{c_k(z)\theta_k(z) + d_k(z)} \quad k = 1, 2, \ldots, M \tag{1.17}$$

$$\theta_k(z) = \frac{-d_k(z)\theta(z) + b_k(z)}{c_k(z)\theta(z) - a_k(z)} \quad k = 1, 2, \ldots, M \tag{1.18}$$

where $\{a_k(z), b_k(z), c_k(z), d_k(z)\}$ can be expressed as,

$$
\begin{pmatrix} a_k(z) & b_k(z) \\ c_k(z) & d_k(z) \end{pmatrix} = \prod_{j=1}^{k} \begin{pmatrix} \frac{z-Y_j}{z-Y_j^*} & \lambda_j^{(j-1)} \\ (\lambda_j^{(j-1)})^* \frac{z-Y_j}{z-Y_j^*} & 1 \end{pmatrix}
\tag{1.19}
$$

here the index j of matrices on the r.h.s. increase from left to right, as the normal order of $\prod$ notation.

In order to get the final expression,

$$
\theta(z)[z; \theta_M(z)] = \frac{a_M(z)\theta_M(z) + b_M(z)}{c_M(z)\theta_M(z) + d_M(z)}
\tag{1.20}
$$

where $\theta_M(Y_M) \in$ B is our parametric function, we use an iterative process as below,

$$
\lambda_1^{(0)} \to \begin{pmatrix} a_1(z) & b_1(z) \\ c_1(z) & d_1(z) \end{pmatrix} \to \lambda_2^{(1)} \to \begin{pmatrix} a_2(z) & b_2(z) \\ c_2(z) & d_2(z) \end{pmatrix} \to \cdots \to \lambda_M^{(M-1)} \to \begin{pmatrix} a_M(z) & b_M(z) \\ c_M(z) & d_M(z) \end{pmatrix}
\tag{1.21}
$$

and use the iterative helper functions ($k = 2, \ldots, M$),

$$
\begin{pmatrix} a_k(z) & b_k(z) \\ c_k(z) & d_k(z) \end{pmatrix} = \begin{pmatrix} a_{k-1}(z) & b_{k-1}(z) \\ c_{k-1}(z) & d_{k-1}(z) \end{pmatrix} \begin{pmatrix} \frac{z-Y_k}{z-Y_k^*} & \lambda_k^{(k-1)} \\ (\lambda_k^{(k-1)})^* \frac{z-Y_k}{z-Y_k^*} & 1 \end{pmatrix}
\tag{1.22}
$$

$$
\lambda_k^{(k-1)} = \theta_{k-1}(Y_k) = \frac{-d_{k-1}(Y_k)\lambda_k + b_{k-1}(Y_k)}{c_{k-1}(Y_k)\lambda_k - a_{k-1}(Y_k)}
\tag{1.23}
$$

Finally, θ is back transformed to a Nevanlinna interpolant via the inverse Möbius transform h^{-1}, $\mathcal{NG}(z) = h^{-1}(\theta(z)) = i\frac{1+\theta(z)}{1-\theta(z)}$. In practice, we found that solving these equations required at least quadruple precision.

1.3 Pick Criterion

Pick independently developed the famous existence criterion for Schur interpolation in 1917 [5, 6]: if $g(x_i) = y_i$ ($x_i \in \mathcal{D}$, $y_i \in \overline{\mathcal{D}}$; $i = 1, 2, \ldots$), Schur interpolants to $g(z)$ can be found if and only if the Pick matrix,

$$
\left[\frac{1 - y_i y_j^*}{1 - x_i x_j^*} \right]_{i,j}
\tag{1.24}
$$

is positive semi-definite. It has a unique solution if furthermore the Pick matrix is singular.

Generalizing Pick criterion gives us a straightforwardly verifiable criterion for the existence of Nevanlinna interpolants directly based on input data. Nevanlinna interpolants exist if and only

if the conformal Pick matrix,

$$\left[\frac{1 - \lambda_i \lambda_j^*}{1 - h(Y_i)h(Y_j)^*}\right]_{i,j} \quad i,j = 1, 2, \ldots, M \tag{1.25}$$

is positive semi-definite; and a unique solution only if it is singular. h is the Möbius transform, Y_i and λ_i are defined in (1.6). In practice, we find that most noisy data (in particular most Monte Carlo data) does not satisfy this criterion, meaning that there does not exist a globally positive and holomorphic function in the upper half plane that passes through all Matsubara points.

1.4 Hamburger Moment Problem

The truncated Hamburger moment problem (HM) looks for a non-decreasing measure $\sigma(\omega)$ on the real line $\mathbb{R}$ such that,

$$h_k = \int_{-\infty}^{\infty} \omega^k d\sigma(\omega) \quad k = 0, 1, 2, \ldots, 2N - 2 \tag{1.26}$$

where N is any positive integer and $b = (h_0, h_1, h_2, \ldots, h_{2N-2})$ is a given real vector.

The Hamburger-Nevanlinna theorem [7] establishes a one to one correspondence between the class of solutions $\sigma(\omega)$ (if they exist) to a subset of the Nevanlinna function class N. For a given solution $\sigma(\omega)$,

$$f(z) = \int_{-\infty}^{\infty} \frac{d\sigma(\omega)}{\omega - z} \quad z \in \mathcal{C}^+ \tag{1.27}$$

belongs to N. And this Nevanlinna function $f(z)$ admits an asymptotic expansion (as $|z| \to \infty$ uniformly inside any angle $\epsilon < arg\ z < \pi - \epsilon$ for some $0 < \epsilon < \frac{\pi}{2}$),

$$f(z) = -\frac{h_0}{z} - \frac{h_1}{z^2} - \frac{h_2}{z^3} - \cdots - \frac{h_{2N-2}}{z^{2N-1}} - o\left(\frac{1}{z^{2N-1}}\right) \tag{1.28}$$

Therefore, HM problem provides us another approach to restore Nevanlinna function $\mathcal{NG}$. We obtain the Nevanlinna interpolant $f(z)$ of $\mathcal{NG}$ by the moment vector $b = (h_0, h_1, h_2, \ldots, h_{2N-2})$ of its measure function $\sigma(\omega)$ (correlated by 1.27) which involves the first $2N - 1$ moments.

Moments $h_0, h_1, h_2, \ldots$ of the measure function $\sigma(\omega)$ corresponding to $\mathcal{NG}(z)$ theoretically can be found by Fourier transforming $\mathcal{G}(i\omega_n)$ where $\omega_n \to \infty$,

$$\mathcal{NG}(i\omega_n) = -\mathcal{G}(i\omega_n) \tag{1.29}$$

$$= -\int_0^\beta d\tau \mathcal{G}(\tau)e^{i\omega_n \tau} \tag{1.30}$$

$$= -\sum_{k=0}^{\infty} \frac{(-1)^{k+1}(\mathcal{G}^{(k)}(\beta) + \mathcal{G}^{(k)}(0))}{(i\omega_n)^{k+1}} \tag{1.31}$$

$$= -\frac{h_0}{i\omega_n} - \frac{h_1}{(i\omega_n)^2} - \frac{h_2}{(i\omega_n)^3} - \cdots \tag{1.32}$$

and where the (1.30) to (1.31) transformation is accomplished by partial derivative [8]. In practice, the moments can be extracted from the so-called equation of motion and are typically well known because they encapsulate perturbative short-time physics.

Few lines of derivation further gives $A(\omega) = \frac{d\sigma(\omega)}{d\omega}$, where $\sigma(\omega)$ is the measure function corresponding to the Nevanlinna function $\mathcal{N}\mathcal{G}$. Non-decreasing $\sigma(\omega)$ in moment theory acts like a cumulative distribution function and therefore its derivative acts like a density distribution function, which corresponds with the single particle density of states measuring effect of $A(\omega)$.

Proof.

$$\mathcal{N}\mathcal{G}(z) = -\mathcal{G}(z) = \int_{-\infty}^{\infty} d\omega \frac{A(\omega)}{\omega - z} = \int_{-\infty}^{\infty} \frac{d\sigma(\omega)}{\omega - z} \tag{1.33}$$

$$A(\omega) = \frac{d\sigma(\omega)}{d\omega} \geqslant 0 \tag{1.34}$$

$\square$

We use the well-known method to solve the truncated Hamburger Moment problem [7, 9]. First formulate the famous Hankel matrix,

$$H_{kl}[b] = (h_{i+j})_{i,j=0}^{i=k-1,j=l-1} \quad k + l = 2N \tag{1.35}$$

where $b = (h_0, h_1, h_2, \ldots, h_{2N-2})$ is the moment vector.

Denote a general matrix $A \geq 0$ if it is positive semi-definite, and $A > 0$ if it is positive definite; call it proper [10] if the leading submatrix (in the top-left corner) of order $n_1 \times n_1$ is non-singular. For a proper Hankel matrix, let $n_2 = 2N - n_1$ and obviously $n_1 \leq n_2$. Note that any matrix $A > 0$ is non-singular and thus proper, and that the matrix A is singular if $A \geq 0$ but is not > 0.

One kind of polynomial space related to the kernel of Hankel matrices is used,

$$\mathcal{A}_l = (1, z, z^2, \ldots, z^{l-1}) ker(H_{kl}[b]) \quad k + l = 2N \tag{1.36}$$

Then two kinds of polynomials are formulated with respect to the Hankel matrix $H_{NN}[b]$.

$p(z)$ and $q(z)$ are the first kind of polynomials. They are called the canonical pair of characteristic polynomials of the vector b. They are defined in the following way. If $n_1 = n_2 = N$, according to rank–nullity theorem, $\mathcal{A}_{n_1+1}$ has dimension 2. $p(z)$ and $q(z)$ form a basis of $\mathcal{A}_{n_1+1}$. Otherwise $n_1 < n_2$, $\mathcal{A}_{n_1+1}$ has dimension 1. $p(z)$ form a basis of $\mathcal{A}_{n_1+1}$, while $p(z), \lambda p(z), \ldots, \lambda^{n_2-n_1} p(z), q(z)$ form a basis of $\mathcal{A}_{n_2+1}$.

For convenience, use the special canonical pair polynomials $p(z)$ and $q(z)$ of b. They are in essence orthogonal polynomials of an infinite positive sequence, extended from the longest positive subsequence (starting from the beginning) of b. (A sequence is called positive if it can generate a Hankel matrix that is positive definite.) Or symbolically, we denote the n_1-th order orthogonal polynomial by,

$$\alpha \det \begin{bmatrix} h_0 & h_1 & \cdots & h_{n_1} \\ h_1 & h_2 & \cdots & h_{n_1+1} \\ \vdots & \vdots & & \vdots \\ h_{n_1-1} & h_{n_1} & \cdots & h_{2n_1-1} \\ 1 & z & \cdots & z^{n_1} \end{bmatrix} \tag{1.37}$$

Here, if $n_1 = N$ (h_{2n_1-1} is not given), we let h_{2n_1-1} be an arbitrary real number. And α is the normalization coefficient that makes coefficient of z^{n_1} to be 1. When $H_{NN}[b] \geq 0$ and is proper, we let the special canonical pair polynomials $p(z)$ be the n_1-th order orthogonal polynomial, and $q(z)$ be the $n_1 - 1$-th order polynomial.

$S(p(z))$ and $S(q(z))$ are the symmetrizers of $p(z)$ and $q(z)$,

$$
S(p(z)) = \begin{pmatrix} p_1 & \cdots & p_{n_1-1} & p_{n_1} \\ \vdots & \ddots & \ddots & 0 \\ p_{n_1-1} & \ddots & \ddots & \vdots \\ p_{n_1} & 0 & \cdots & 0 \end{pmatrix}, \; S(q(z)) = \begin{pmatrix} q_1 & \cdots & q_{n_2-1} & q_{n_2} \\ \vdots & \ddots & \ddots & 0 \\ q_{n_2-1} & \ddots & \ddots & \vdots \\ q_{n_2} & 0 & \cdots & 0 \end{pmatrix}
\tag{1.38}
$$

$\gamma(z)$ and $\delta(z)$ are the second kind of polynomials. They are conjugate polynomials of $p(z)$ and $q(z)$,

$$
\gamma(z) = (1, z, z^2, \ldots, z^{n_1-1}) S(p(z)) (h_0, h_1, \ldots, h_{n_1-1})^{\mathsf{T}}
\tag{1.39}
$$

$$
\delta(z) = (1, z, z^2, \ldots, z^{n_2-1}) S(q(z)) (h_0, h_1, \ldots, h_{n_2-1})^{\mathsf{T}}
\tag{1.40}
$$

Finally, solutions of HM problem (1.26) comes as follows. HM problem has a solution if and only if $H_{NN}[b] \geq 0$ is proper. There are thus two cases. When $H_{NN}[b] > 0$ The solution class is given by,

$$
f(z) = \int_{-\infty}^{\infty} \frac{d\sigma(\omega)}{\omega - z} = -\frac{\gamma(z) + \varphi(z)\delta(z)}{p(z) + \varphi(z)q(z)}
\tag{1.41}
$$

where $\varphi(z)$ is any Nevanlinna function such that $\varphi(z)/z \to 0$ as $|z| \to \infty$. When $H_{NN}[b] \geq 0$ is singular and proper, HM problem has a single rational solution,

$$
f(z) = \int_{-\infty}^{\infty} \frac{d\sigma(\omega)}{\omega - z} = -\frac{\gamma(z)}{p(z)}
\tag{1.42}
$$

which is real on the real axis. We remark that $\varphi(z)$ defines an embedded Nevanlinna interpolation problem whose values at Matsubara nodes are fixed by (1.41) and Matsubara frequency Green's function values (if given), thus Hamburger Moment problem can be combined with Schur method.

1.5   Hardy Basis Optimization

In the final Schur's continued fraction expansion (1.20), the choice of θ_M is still to be discussed. Any contractive function will yield a valid interpolation and spectral function, and therefore this freedom can be used to select the 'best' of all consistent spectral functions. It is natural to expand θ_M into a set of basis functions and optimize the resulting spectral function in some norm as a function of those basis function coefficients. As we demonstrate in "Results", a constant θ_M results in spectral functions with oscillations. We therefore employ the freedom in choosing θ_M to eliminate these oscillations and obtain the smoothest possible spectral function. Other criteria, such as proximity to a trial function that is either featureless or exhibits a desired feature, are possible but have not been pursued here.
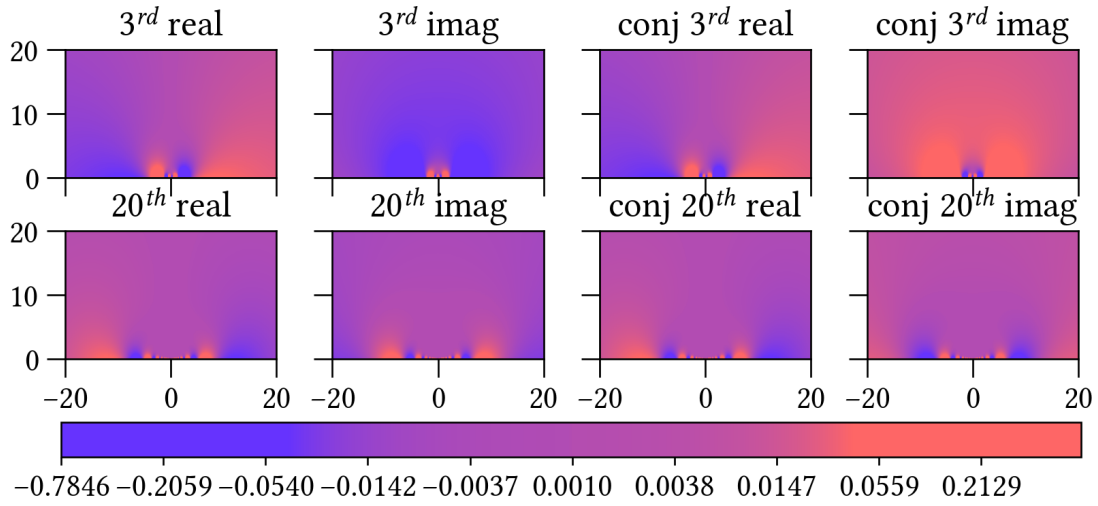
Figure 1.2: Real and imaginary parts of the 3rd and 20th Hardy functions and conjugates used in the optimization, plotted in the upper half complex plane.

First, Hardy space H^2 for $\mathcal{C}^+$ is the space of holomorphic functions on $\mathcal{C}^+$ with bounded quasi-norm,

$$\|f\|_{H^2} = sup_{\eta>0} \left(\int |f(\omega + i\eta)|^2 \right)^{\frac{1}{2}} < \infty \tag{1.43}$$

H^2 space basis are,

$$B^k(z) = \{ \frac{1}{\sqrt{\pi}(z+i)} \left(\frac{z-i}{z+i} \right)^k \}_{k\in\mathbb{N}} \tag{1.44}$$

In fact, holomorphic f and bounded quasi-norm makes the integral in (1.43) nonincreasing as a function of $\eta \in (0,\infty)$. Hence we can replace $sup_{\eta>0}$ by $\lim_{\eta\to0^+}$ [11]. This means all H^2 functions are square integrable on our evaluation axis $\omega + i\eta$, i.e., have $o(\omega^{-2})$ decay as $|\omega| \to \infty$, while rapid variations exist between them at low $|\omega|$ region.

We use truncated Hardy space basis to generate functions in the contractive function space and feature low frequency variations. We additionally add their conjugate to represent functions more efficiently without exhausting truncation order. This is because real and imaginary part of Hardy basis are correlated while adding conjugate enables them to function independently (See Fig. 1.2). $\theta(M)$ is therefore expanded as,

$$\theta(M) = \sum_{k=0}^{H} a_k B^k(z) + b_k (B^k(z))^* \tag{1.45}$$

Then, we minimize a functional norm w.r.t. $A(\omega)$ to find complex coefficients a_k and b_k,

$$F[A_{\theta_M}(\omega)] = \left| 1 - \int A_{\theta_M}(\omega)d\omega \right|^2 + \lambda \left\| \frac{d^2 A_{\theta_M}(\omega)}{d\omega^2} \right\|^2 \tag{1.46}$$
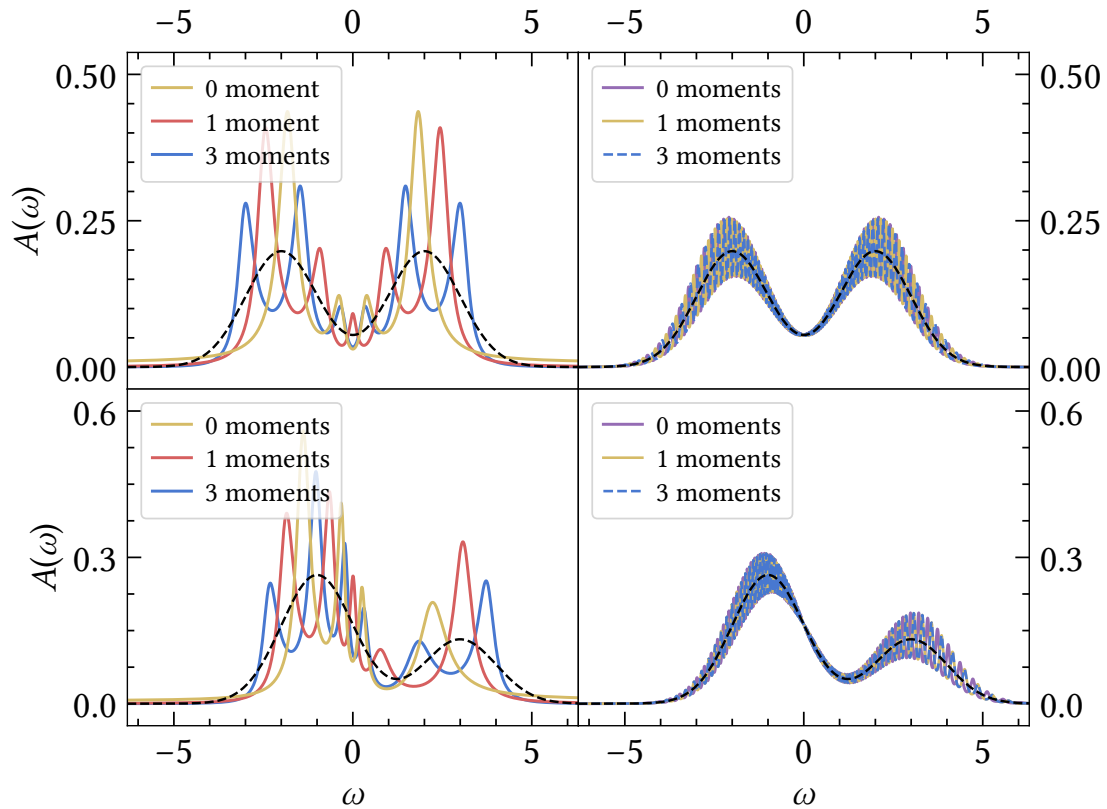
Figure 1.3: Schur algorithm combined with Hamburger Moment Problem (without optimization). Uniform grid $\omega_n = (2n+1)\pi/\beta \quad n = 0, 1, 2 \ldots, M-1$ with $M = 5, \beta = 10$ (left) and $M = 101, \beta = 200$ (right).

where $\|\cdot\|$ denotes a L^2 integral norm. The first term enforces proper normalization, while the second term promotes smoothness by minimizing second derivatives (we typically use $\lambda = 10^{-4}$ and $H = 25$). Second order derivative of f was done in the reciprocal space using fast Fourier transform (FFT). λ can be tuned for better performance.

Finally, we used a conjugate gradient minimizer of the Dakota package [12] to minimize the norm and eliminate oscillations from the spectral function. For practical convenience, we used unconstrained optimization. The contractive condition $|\theta_M(z)| \leqslant 1$ for $z \in \mathcal{C}^+$ would be enforced by the program as long as Nevanlinna solutions exist. Because in that case the smoothest $A(\omega)$ always corresponds to a Nevanlinna interpolant which requires a contractive parametric function $\theta_M(z)$.

Nevertheless, we will show in "Results" section that in most practical cases with less than double input data precision, Nevanlinna interpolants to $\mathcal{NG}$ don't exist. But the Schur continued fraction expansion still builds up structures closest to Nevanlinna functions with $a(z)$, $b(z)$, $c(z)$ and $d(z)$ faithful to input, and with $\theta(z)$ adapted by the unconstrained optimization program while no longer guaranteed to be contractive.
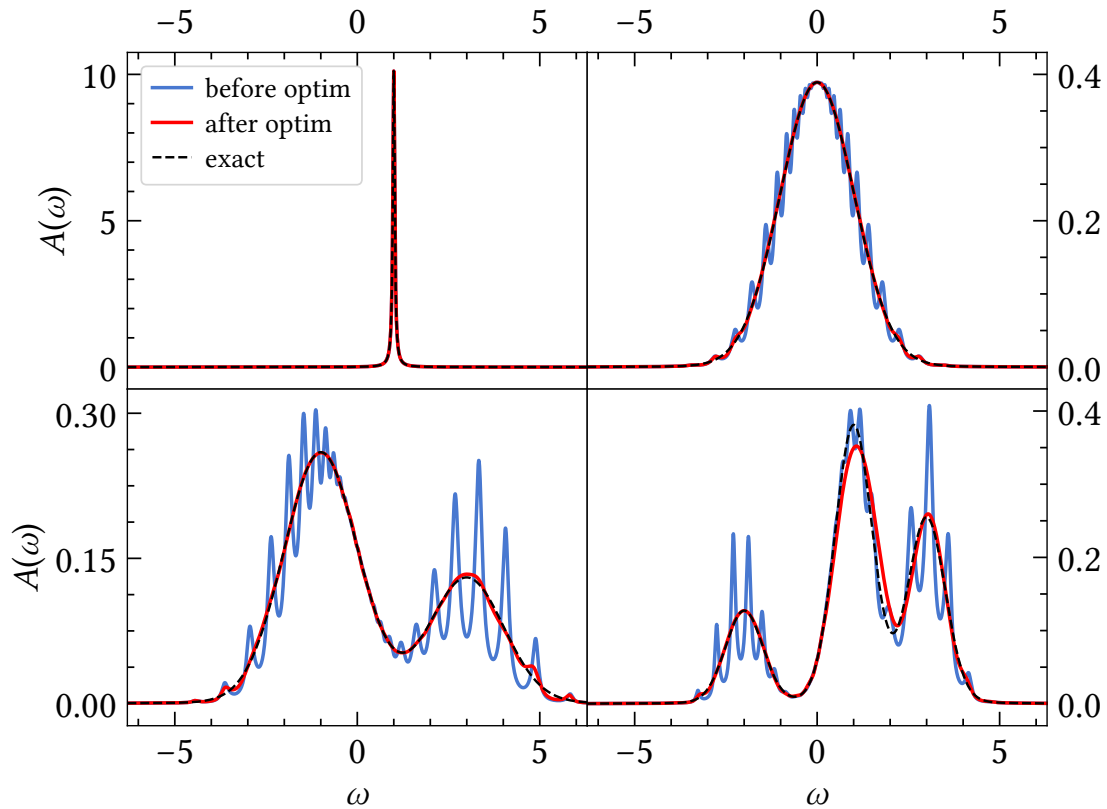
Figure 1.4: Continuation with and without Hardy function optimization. Off-centered δ peak (top left), Gaussian (top right), two-peak scenario (bottom left), and a three-peak scenario (bottom right). $\beta = 100$, IR grid [13, 14] with 36 Matsubara positive frequency points.

1.6 Results

1.6.1 Effects of Moments

Fig. 1.3 demonstrate the effect of enforced moments (Hamburger Moment method in combination with Schur algorithm; 1 and 3 moments, which can be obtained in quantum simulation with good accuracies) by comparison with bare Schur method (0 moment). The interpolation is done with double precision input data and $\theta_M = 0$ constant parametric function. We show that for very few Matsubara points (5 points in the left panel), moments indeed add additional information and fix the shape to some extent. However, since moment information are already carried asymptotically in the high frequency samplings of Matsubara data with precision, enforced moments do not yield advantage when number of input points are enough (101 points in the right panel). A combination may become useful if fits to noisy Monte Carlo data are attempted.

1.6.2 Effects of Optimization

Results of following sections were all generated with Schur algorithm and Hardy basis opimization techniques. Fig. 1.4 shows the results for four prototypical spectral functions: an off-center δ-peak 'level' (top left), a centered Gaussian (top right), a double-peak 'pseudogap' scenario (bottom left), and a three-peak structure with a second, smaller peak hidden behind the first peak.
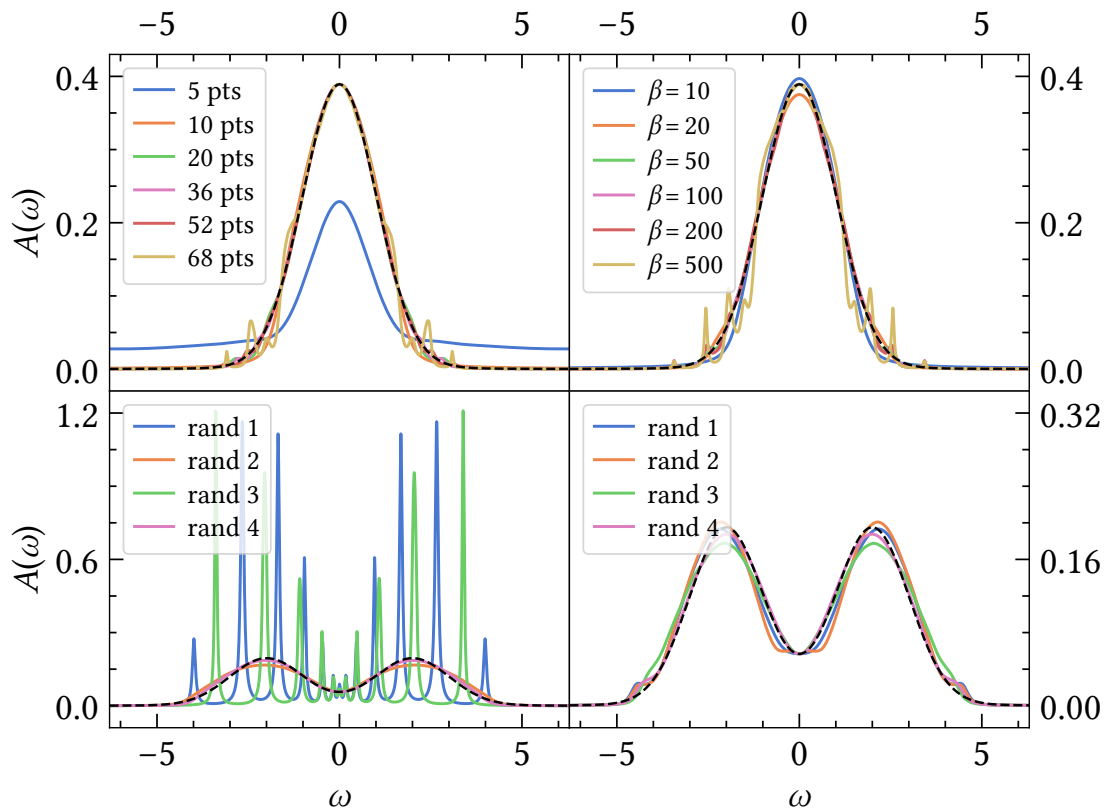
Figure 1.5: Top left: effect of the number of interpolation nodes (IR grid [13, 14]) used. Top right: effect of Matsubara spacing (inverse temperature), uniform grid $\omega_n = (2n + 1)\pi/\beta$ used. Bottom two panels: effect of independent Gaussian noise with relative standard deviation of 10^{-4} (left) and 10^{-6} (right), four sample curves each.

Black lines show input data that is then back-continued to the imaginary axis in double precision as an input for the interpolation algorithm.

   We show two sets of results from Nevanlinna continuation which both interpolate all Matsubara points and are intrinsically positive and normalized. First, the result of an interpolation using a constant function $\theta_M = 0$. For the δ-function, the interpolation is very close to the original data. However, other curves display artificial oscillations. The number of these oscillations increases as additional Matsubara points are fit. Nevertheless, the approximate shape of the original spectral function is evident in all interpolations.

   Next, we exploit the additional freedom to find the 'best' function among all possible interpolants by minimizing the functional $F[A_{\theta_M}(\omega)]$ with 25 Hardy basis coefficients and their conjugates. Other choices of functionals, including minimizing $\int A'(\omega)$ while keeping $\int A(\omega)$ constant, yield similar results. As is evident in Fig. 1.4, the minimization eliminates all oscillations and produces a spectral function that is both smooth and very close to the original data, while not destroying the sharp features of the δ peak in the top left panel.

1.6.3   Effects of Number of Points, Beta and Noise

Fig. 1.5 illustrates the robustness of the procedure. As additional Matsubara points are added (top left), the function converges rapidly to the correct result. If too many points are provided,
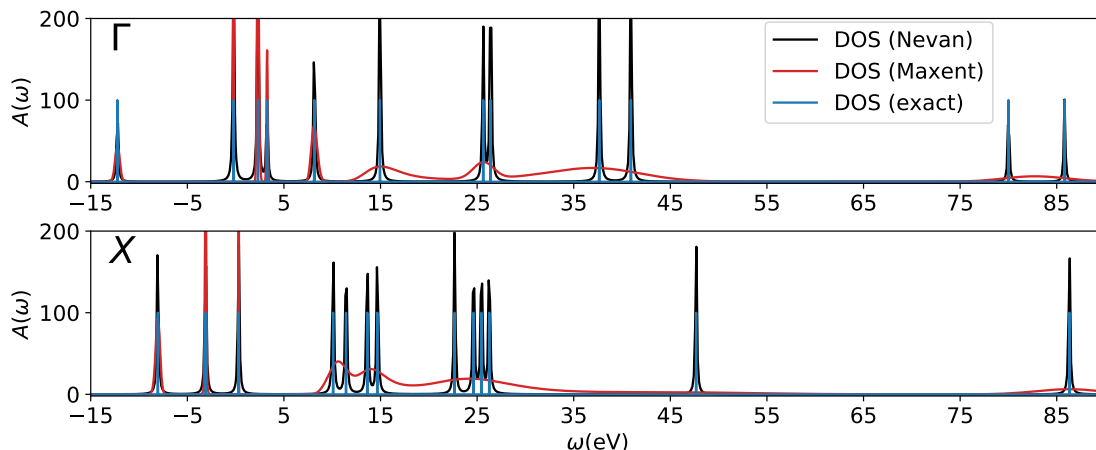
Figure 1.6: LDA band structure (Kohn Sham eigenvalues, DOS) of solid Si (green) at the Γ and the X point, as well as Nevanlinna (blue) and MaxEnt (orange) continuations of the corresponding Green's functions. T=316 K, 52 non-uniform [14] IR Basis [13] Matsubara positive frequency points.

the minimization routine struggles with finding an appropriate global minimum and does not completely eliminate all oscillations. Varying the position of the Matsubara sampling points (top right, large β corresponds to low T and sampling points close to the real axis, physical maximum frequency is kept constant such that the number of sampling points increases from 5 to 253) again illustrates the difficulty of optimizing very many degrees of freedom.

Finally, the lower two panels show the effect of noise (such as Monte Carlo noise from a quantum Monte Carlo simulation [15, 16]) on the input data. Shown are four traces with independent Gaussian noise on the input data (left panel: 10^{-4} relative noise. right panel: 10^{-6}). It is evident that even small noise forces large deviations of the interpolation from the unperturbed spectral function. This is a sign of the ill conditioned nature of the continuation kernel, as well as of the sensitivity of the interpolation to high frequency data. Remarkably, even though none of the functions with noise satisfy the Nevanlinna criterion (Eq. 1.25), the interpolation recovers a reasonable approximation to the spectral function. The fact that Eq. 1.25 is almost never satisfied for noisy data implies that a fit, rather than an interpolation, should be used for continuation of noisy data.

1.6.4   Real Material Examples

We now turn to Fig. 1.6. Shown are k-resolved DFT Kohn Sham eigenvalues (the 'band structure') of solid Si in the LDA approximation at the Γ and the X point, obtained on an $8 \times 8 \times 8$ grid in the *gth-dzvp-molopt-sr* basis [17] with *gth-pbe* pseudopotential [18]. The eigenvalue spectrum at the k-points shown is back-continued to the Matsubara axis in double precision, at $T = 316K$ and with 52 non-uniform [14] IR Basis [13] Matsubara points, for each orbital individually, and then analytically continued. Shown are Nevanlinna (blue) and Maximum Entropy continuations (orange). It is evident that Nevanlinna resolves the delta peaks at the right locations, even at very high energy, whereas MaxEnt only obtains the approximate area, but not the sharp unperturbed levels at high energy. Continuations of this type often appear in correlated simulations of real materials, where the spectral function broadening due to electron correlations needs to be distinguished from a broadening due to analytic continuation deficiencies. Our method, which is able to capture both broad features near the Fermi energy and sharp features away from it, therefore offers the unique capability of accurately resolving bandstructure at high energy. The fact that

sharp features are resolved, despite Hardy function smoothing, hints at the severe restriction of the functions available within the Nevanlinna space.
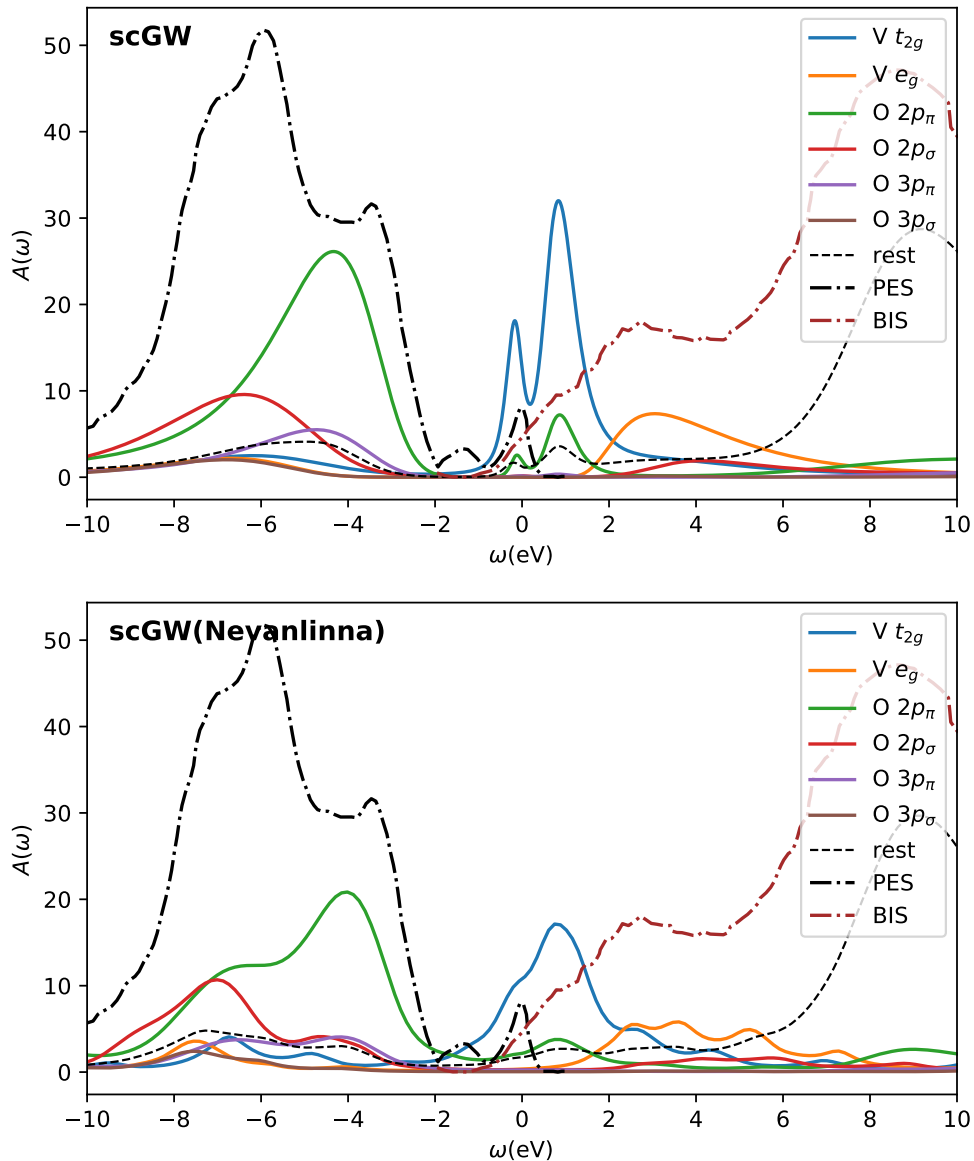

Figure 1.7: Orbital-resolved realistic band structure of $SrVO_3$ from self-consistent GW continued with MaxEnt (top) and with Nevanlinna (bottom) [19].

To illustrate the power of the method in a difficult realistic correlated setting, we show near-Fermi-energy results from a self-consistent GW [20] calculation of $SrVO_3$ in Fig. 1.7, from Max-Ent (top) [21] and Nevanlinna (bottom panel). For methods details and physics discussion see Ref. [19]. Shown are experimental photoemission [22] and bremsstrahlung isochromat spectroscopy [23] data along with orbitally resolved local GW spectra obtained at $T = 1579K$ on a $6 \times 6 \times 6$ grid in a Gaussian *gth-dzvp-molopt-sr* basis [17] with *gth-pbe* pseudopotential [18] at 84 frequency points. The four-fermion Coulomb integrals are decomposed into a combination of

auxiliary even-tempered Gaussian for Strontium and *def2-svp-ri* [24] bases for all other atoms. Both methods recover the same overall features. However, Nevanlinna continuation reveals additional details such as multiplet structures in the occupied and unoccupied bands, and does not exhibit artificial oscillations in the t_{2g} bands near the Fermi energy.
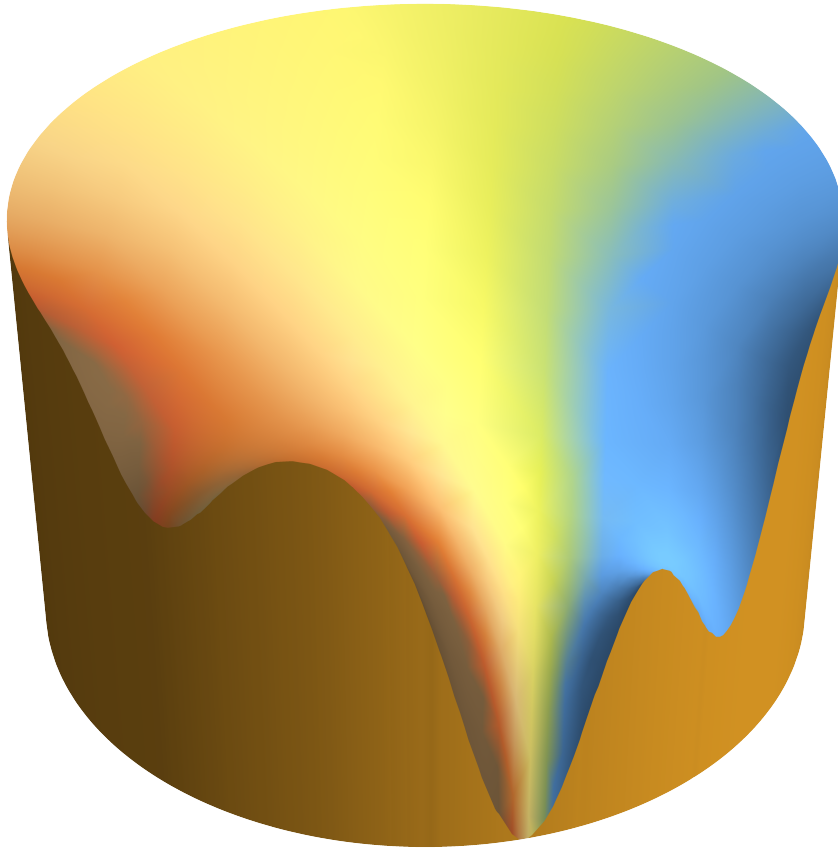

Figure 1.8: The Nevanlinna work was selected as Editors' Suggestion and showed up on the *Physical Review Letters* homepage. This logo is the Nevanlinna structure of a typical three-peak spectral function that is mapped to the unit circle. The color scheme corresponds to the real part of the function. Credit to Jiani Fei and Emanuel Gull.

Chapter 2

Matrix-valued Response Functions

2.1 Carathéodory Function Definition

Carathéodory class of matrix-valued analytic functions in the unit disk is defined as $C = \{M(z) : M(z) + M^\dagger(z) \geq 0 \text{ for } |z| < 1\}$ [25, 26], where M is a $m \times m$ square matrix, and a matrix $A \geq 0$ denotes A is a positive semi-definite (PSD) matrix as before. Note that $M(z) + M^\dagger(z) \geq 0$ is the same as saying $\text{Re}\{x^\dagger M(z)x\} \geq 0$ for any complex vector x of length m, because

$$x^\dagger(M + M^\dagger)x = x^\dagger Mx + x^\dagger M^\dagger x \tag{2.1}$$

$$= x^\dagger Mx + (x^\dagger Mx)^\dagger \tag{2.2}$$

$$= 2\text{Re}\{x^\dagger Mx\} \geq 0 \tag{2.3}$$

2.2 $-iG^<(\omega)$ is PSD

By Lehmann representation, the lesser Green's function has entries,

$$G_{ij}^<(\omega) = 2\pi i \sum_{mn} \frac{e^{-\beta E_n}}{Z} \langle n|c_j^\dagger|m\rangle \langle m|c_i|n\rangle \delta(\omega - E_n + E_m) \tag{2.4}$$

where E_m and E_n are eigenvalues corresponding to the eigenstates $|m\rangle$ and $|n\rangle$ of a Hamiltonian, $Z = \sum_m e^{-\beta E_m}$ is the partition function, β is the inverse temperature, $c_i^\dagger$ is the creation operator for the spin-orbital $i = (i, \sigma)$ and c_i is the annihilation operator.

We prove that $-iG^<(\omega)$ is a positive semi-definite (PSD) matrix for any ω. For any complex vector $|x\rangle$,

$$\langle x|-iG^<(\omega)|x\rangle = 2\pi \sum_{mnij} \frac{e^{-\beta E_n}}{Z} \langle n|c_j^\dagger x_j|m\rangle \langle m|c_i x_i^*|n\rangle \delta(\omega - E_n + E_m) \tag{2.5}$$

$$= 2\pi \sum_{mn} \frac{e^{-\beta E_n}}{Z} \langle n|\sum_j c_j^\dagger x_j|m\rangle \langle m|\sum_i c_i x_i^*|n\rangle \delta(\omega - E_n + E_m) \tag{2.6}$$

$$= 2\pi \sum_{mn} \frac{e^{-\beta E_n}}{Z} \langle m|\sum_i c_i x_i^*|n\rangle^2 \delta(\omega - E_n + E_m) \geq 0 \tag{2.7}$$

2.3 $iG^>(\omega)$ is PSD

The greater Green's function has entries,

$$G^>_{ij}(\omega) = -2\pi i \sum_{mn} \frac{e^{-\beta E_n}}{Z} \langle n|c_i|m\rangle\langle m|c_j^\dagger|n\rangle \delta(\omega + E_n - E_m) \tag{2.8}$$

We prove that $iG^>(\omega)$ is a PSD matrix for any ω. For any complex vector $|x\rangle$,

$$\langle x|iG^>(\omega)|x\rangle = 2\pi i \sum_{mnij} \frac{e^{-\beta E_n}}{Z} \langle n|c_i x_i^*|m\rangle\langle m|c_j^\dagger x_j|n\rangle \delta(\omega + E_n - E_m) \tag{2.9}$$

$$= 2\pi i \sum_{mn} \frac{e^{-\beta E_n}}{Z} \langle n|\sum_i c_i x_i^*|m\rangle\langle m|\sum_j c_j^\dagger x_j|n\rangle \delta(\omega + E_n - E_m) \tag{2.10}$$

$$= 2\pi i \sum_{mn} \frac{e^{-\beta E_n}}{Z} \langle n|\sum_i c_i x_i^*|m\rangle^2 \delta(\omega + E_n - E_m) \geq 0 \tag{2.11}$$

2.4 $i\mathcal{G}(z)$ is Carathéodory

The matrix-valued Green's function $\mathcal{G}(z)$ restricted to the upper half complex plane $\mathcal{C}^+$ has entries,

$$\mathcal{G}_{ij}(z) = \frac{1}{Z} \sum_{m,n} \frac{\langle n|c_i|m\rangle\langle m|c_j^\dagger|n\rangle}{z + E_n - E_m}(e^{-\beta E_n} + e^{-\beta E_m}) \tag{2.12}$$

We prove for $z \in \mathcal{C}^+$, $i\mathcal{G}(z) + (i\mathcal{G}(z))^\dagger$ is a PSD matrix, i.e., $i\mathcal{G}(z)$ is a Carathéodory class function on $\mathcal{C}^+$. For any complex vector $|x\rangle$,

$$\langle x|i\mathcal{G}(z) + (i\mathcal{G}(z))^\dagger|x\rangle = \frac{1}{Z} \sum_{mnij} \left[\frac{i(e^{-\beta E_m} + e^{-\beta E_n})}{z + E_n - E_m} - \frac{i(e^{-\beta E_m} + e^{-\beta E_n})}{z^* + E_n - E_m}\right] \langle n|c_i x_i^*|m\rangle\langle m|c_j^\dagger x_j|n\rangle \tag{2.13}$$

$$= \frac{1}{Z} \sum_{mn} \left[\frac{i(e^{-\beta E_m} + e^{-\beta E_n})}{z + E_n - E_m} - \frac{i(e^{-\beta E_m} + e^{-\beta E_n})}{z^* + E_n - E_m}\right] \langle n|\sum_i c_i x_i^*|m\rangle^2 \tag{2.14}$$

$$= \frac{1}{Z} \sum_{mn} \frac{2\text{Im}\{z\}\,(e^{-\beta E_m} + e^{-\beta E_n})}{\text{Im}\{z\}^2 + (\text{Re}\{z\} + E_n - E_m)^2} \langle n|\sum_i c_i x_i^*|m\rangle^2 \geq 0 \tag{2.15}$$

2.5 $i\Sigma(z)$ is Carathéodory

The fantastic idea of the Lehmann representation of self-energy comes from two outstanding papers, Ref. [27] and [28]. We have extended them to the direct proof of $i\Sigma(z)$ being Carathéodory.

Derivation stems from the construction of an effective non-interacting Hamiltonian with respect to an arbitrary interacting Hamiltonian [27, 28]. Effectiveness lies in the Green's function (same on the physical orbitals) and self-energy (differed by a Hartree-Fock-like term).
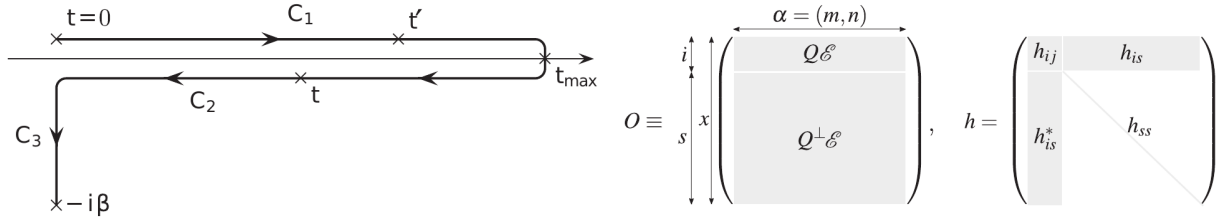
Figure 2.1: Left: Keldysh-Matsubara contour C. In this case $t >_C t'$ in the text. Right: Unitary completion of the time-dependent Matrix $Q(t)$. The matrix $Q^\perp(t)$ contains a completing set of orthonormal basis vectors in its rows. The phase factor ε is absorbed. The generating Hermitian matrix $h(t)$ can be assumed to be diagonal in the virtual sector [28]

.

A general time-dependent and fermionic model Hamiltonian can be,

$$H(t) = \sum_{ij}[T_{ij}(t) - \mu\delta_{ij}]c_i^\dagger(t)c_j(t) + \frac{1}{2}\sum_{iji'j'}U_{ii'jj'}(t)c_j(t)c_{i'}^\dagger(t)c_{j'}(t)c_i(t) \qquad (2.16)$$

where $c_i(t) = U^\dagger(t,0)c_i U(t,0)$, $U(t,t') = \mathcal{T}_C \exp(-i\int_t^{t'} H(t_1)dt_1)$ is the system's time-evolution operator and $\mathcal{T}_C$ is the time-ordering operator along the Keldysh-Matsubara contour (see Fig. 2.1 left panel).

The non-equilibrium Green's function can be expanded by Lehmann representation as [29],

$$\mathcal{G}_{ij}(t,t') = \sum_{\alpha} Q_{i\alpha}(t)g(\epsilon_\alpha;t,t')Q_{j\alpha}^*(t') \qquad (2.17)$$

where

$$g(\epsilon;t,t') = i[\frac{1}{e^{\beta\epsilon}+1} - \Theta_C(t,t')]e^{i\epsilon(t-t')} \qquad (2.18)$$

$[\Theta_C(t,t') = 1$ for $t \geqslant_C t'$, $\Theta_C(t,t') = 0$ otherwise$]$ is the non-interacting Green's function of an isolated one-particle mode ($h_{\text{mode}} = \epsilon c^\dagger c$) with excitation energy ϵ, and

$$Q_{i\alpha}(t) = Q_{i(m,n)}(t) = \sqrt{\frac{e^{-\beta E_m} + e^{-\beta E_n}}{Z}}\langle m|c_i(t)|n\rangle e^{i\epsilon_{(m,n)}t} \qquad (2.19)$$

where m and n are some states for tracing over the Fock space (here for example the eigenstates of the initial Hamiltonian H_{ini}). The index $\alpha = (m,n)$ labels the possible one-particle excitation with corresponding excitation energy $\epsilon_\alpha = \epsilon_{(m,n)} = E_m - E_n$.

Construction of the effective non-interacting Hamiltonian follows from Eqn. 2.17 [28]. Since $\Sigma = \mathcal{G}_0^{-1} - \mathcal{G}^{-1}$ needs the inversion of $\mathcal{G}$ which in turns needs a quadratic form, the row-orthonormal matrix $Q(t)$ is completed into the orthonormal square matrix $O(t)$. The phase factor $\varepsilon_{\alpha\alpha'} = \delta_{\alpha\alpha'}\exp(-i\varepsilon_\alpha t)$ is absorbed into $O(t)$ from $g(\epsilon_\alpha;t,t')$ for convenience (see Fig. 2.1 right panel).

Define

$$h_{xy}(t) = \sum_{\alpha}[i\partial_t O_{x\alpha}(t)]O_{\alpha y}^\dagger(t), \qquad (2.20)$$

the effective Hamiltonian is then,

$$H_{\text{eff}}(t) = \sum_{xy} h_{xy}(t) c_i^\dagger c_j \tag{2.21}$$

where the virtual part is chosen to be diagonal and time-independent $h_{ss'}(t) = h_{ss}(0)\delta_{ss'}$. This requirement defines H_{eff} uniquely up to a rotations in invariant subspace ($O(t)$ should be chosen to match).

From some proofs (Ref. [28]) it was shown that the Green's function of this effective Hamiltonian in the physical sector exactly equals the Green's function of the original interacting Hamiltonian (Eqn. 2.16). And that we can express the self-energy $\Sigma_{ij}(t,t')$ of the original model as

$$\Sigma_{ij}(t,t') = \delta_C(t,t')\Sigma_{ij}^{\text{HF}}(t) + \Sigma_{ij}^C(t,t') \tag{2.22}$$

$$\Sigma_{ij}^{\text{HF}}(t) \equiv 2\sum_{i'j'} U_{ii'jj'}(t)\langle \mathcal{T}_C\, c_{i'}^\dagger(t)c_{j'}(t)\rangle_{H_{\text{eff}}} \tag{2.23}$$

$$\Sigma_{ij}^C(t,t') \equiv \sum_s h_{is}(t) g(h_{ss};t,t') h_{js}^*(t'). \tag{2.24}$$

where s are virtual orbitals. The correlated Σ^C term is the self-energy of the effective model, with the trace over the virtual orbitals simulating the retardation effect of the self-energy. The Hartree-Fock-like term is time-local and the additional term of the original self-energy.

We prove for $z \in \mathcal{C}^+$, $i\Sigma(z) + (i\Sigma(z))^\dagger$ is a PSD matrix, i.e., $i\Sigma(z)$ is a Carathéodory class function on $\mathcal{C}^+$. We Fourier transform Σ^C from time domain to the frequency domain as,

$$\Sigma_{ij}^C(i\omega_n) = \int_0^\beta \Sigma_{ij}^{C,M}(\tau) e^{i\omega_n\tau} d\tau \tag{2.25}$$

$$= \int_0^\beta -i\Sigma_{ij}^C(-i\tau,0) e^{i\omega_n\tau} d\tau \tag{2.26}$$

$$= \int_0^\beta h_{is}(0) h_{js}^*(0) \left(\frac{1}{e^{\beta h_{ss}}+1} - 1\right) e^{-h_{ss}\tau} e^{i\omega_n\tau} d\tau \tag{2.27}$$

$$= \frac{h_{is}(0) h_{js}^*(0)(e^{i\omega_n\beta} - e^{h_{ss}\beta})}{(1+e^{h_{ss}\beta})(h_{ss} - i\omega_n)} \tag{2.28}$$

$$= \frac{h_{is}(0) h_{js}^*(0)}{i\omega_n - h_{ss}} \tag{2.29}$$

$$\Sigma_{ij}^C(z) = \frac{h_{is}(0) h_{js}^*(0)}{z - h_{ss}} \tag{2.30}$$

where $\omega_n = \frac{(2n+1)\pi}{\beta}$ are the fermionic Matsubara frequencies so that $e^{i\omega_n\beta} = -1$. Also taking the fact that $Q(t)$, $O(t)$ and $h(t)$ are invariant on the Matsubara branch.

Finally, we observe that $\Sigma^{\text{HF}}(z)$ is Hermitian and z-independent. Since the self-energy has the property that $\Sigma(x+yi) = (\Sigma(x-yi))^\dagger$ for $x,y > 0$, we will have,

$$i\Sigma_{ij}(z) + (i\Sigma_{ij}(z))^\dagger = i\Sigma_{ij}^C(x+yi) - i\Sigma_{ij}^C(x-yi) \tag{2.31}$$

$$= \frac{2h_{is}(0) h_{js}^*(0) y}{(h_{ss}-x)^2 + y^2} \tag{2.32}$$

where $\Sigma_{ij}^{\mathrm{HF}}(x + yi)$ and $\Sigma_{ij}^{\mathrm{HF}}(x - yi)$ cancel out. Therefore, for any complex vector $|x\rangle$,

$$\langle x|i\Sigma(z) + (i\Sigma(z))^\dagger|x\rangle = \frac{2y(\sum_i x_i h_{is}(0))^2}{(h_{ss} - x)^2 + y^2} \geqslant 0 \tag{2.33}$$

2.6 $iM(z)$ **is Carathéodory**

Cumulant M is a derived object that has the properties of a Green's function but lacks the 'Fock' contribution of the one-body Hamiltonian [30, 31]. It has the definition of,

$$M^{-1}(z) = G^{-1}(z) + F \tag{2.34}$$

where F is the Fock matrix. We can relate it with the Green's function as,

$$-iG^{-1}(z) + i(G^{-1}(z))^\dagger = -iM^{-1}(z) + iF + i(M^{-1}(z))^\dagger - iF^\dagger \tag{2.35}$$
$$= -iM^{-1}(z) + i(M^{-1}(z))^\dagger \tag{2.36}$$
$$\tag{2.37}$$

Since F is a Hermitian constant matrix, and that inversion of a matrix-valued function is Carathéodory function if and only if this function itself is, we get $iM(z)$ is a Carathéodory function.

2.7 **Carathéodory Continuation**

To interpolate the Carathéodory class function $i\mathcal{G}(z)$ or $i\Sigma(z)$ restricted to the upper half complex plane $\mathcal{C}^+ = \{z : \mathrm{Im}(z) > 0\}$, we use the matrix extension of Schur algorithm [25, 26, 32] for the classical Nevanlinna-Pick interpolation problem. Schur class of matrix-valued analytic function is defined as $S = \{M(z) : \|M\| \leq 1 \text{ for } |z| < 1\}$, where for this section $\|M\|$ denotes the spectral norm of the matrix M, i.e., the largest singular value of matrix M.

First of all, we transform the Carathéodory interpolation problem on $\mathcal{C}^+$ into a Schur class function interpolation problem on the unit disk $\mathcal{D} = \{z : |z| < 1\}$ by transforming the input: Möbius transform the domain, $h : \mathcal{C}^+ \to \mathcal{D}, z \to \frac{z-i}{z+i}$ and then conformally map the function value, $\Psi(z) = [I - F(z)][I + F(z)]^{-1}$ where $F \in C$ and $\Psi \in S$ [25, 26]. Therefore, given $F(z) = i\mathcal{G}(z)$ or $F(z) = i\Sigma(z)$, $F(x_i) = Y_i$ for $i = 0, 2, \ldots, n - 1$ and Y_i $m \times m$ matrices, we look for the Schur class interpolant $\Psi(z)$ such that

$$\Psi(z_i) = J_i = \Psi(\frac{x_i - i}{x_i + i}) = [I - Y_i][I + Y_i]^{-1} \quad i = 0, 2, \ldots, n - 1 \tag{2.38}$$

Generalizing the Pick criterion, we get the existence condition [25, 26]. Carathéodory interpolants for the original interpolation problem exist if and only if the Pick matrix,

$$P_C = [\frac{Y_k + Y_l^*}{1 - z_k^* z_l}]_{(mn) \times (mn)} \tag{2.39}$$

or alternatively, the new Pick matrix,

$$P_S = [\frac{I - J_k^* J_l}{1 - z_k^* z_l}]_{(mn)\times(mn)} \tag{2.40}$$

is positive semi-definite; and a unique solution only if they are singular.

One iteration step for a Schur class interpolant $\Psi_i(z)$ comes as follows [25]. Given $\Psi_i(z_i) = W_i$, define matrix-valued function $M(z)$ by

$$y_i M(z) = [I - W_i W_i^\dagger]^{-1/2} [\Psi_i(z) - W_i][I - W_i^\dagger \Psi_i(z)]^{-1}[I - W_i^\dagger W_i]^{1/2} \tag{2.41}$$

where $y_i = |z_i|(z_i - z)/(z_i(1 - z_i^\dagger z))$ and $X^{1/2} = VD^{1/2}V^{-1}$ is the Hermitian square root of $X = VDV^{-1}$. $M(z)$ belongs to S by the Schwarz lemma. Define $\Psi_{i+1}(z)$ by

$$\Psi_{i+1}(z) = [I - K_i K_i^\dagger]^{-1/2}[M(z) - K_i][I - K_i^\dagger M(z)]^{-1}[I - K_i^\dagger K_i]^{1/2} \tag{2.42}$$

where K_i is an arbitrary matrix such that $\|K_i\| < 1$, then $\Psi_{i+1}(z) \in S$ as well. And going backwards, arbitrary $\Psi_{i+1}(z) \in S$ with arbitrary $\|K_i\| < 1$ yields $\Psi_i(z) \in S$ and $\Psi_i(z_i) = W_i$.

Given an interpolation problem $\Psi = \Psi_0$ with n nodes, $\Psi(z_i) = J_i$, $i = 0, 1, \ldots, n - 1$, and a selected matrix K_0, Eq. (2.41) and (2.42) defines an interpolation problem for $n - 1$ nodes $z_1, z_2, \ldots, z_{n-1}$ for Ψ_1. Iterate the procedure on Ψ_1, we get Ψ_2 with prescribed values at $n - 2$ nodes $z_2, \ldots, z_{n-1}$, and finally Ψ_n an arbitrary Schur class matrix-valued function. For convenience, we choose all K_i, $i = 0, 1, \ldots, n - 1$ to be zero matrix, and Ψ_n to be an identity matrix.

Denoting $\Psi_i(z_j) = W_j^i$, $i, j = 0, 1, \ldots, n - 1$ and $W_i^i = W_i$, the first stage of the algorithm is to find out all W_i and store them. By Eq. (2.41) and (2.42), we have

$$W_j^{i+1} = \frac{z_i(1 - z_i^\dagger z_j)}{|z_i|(z_i - z_j)}[1 - W_i W_i^\dagger]^{-1/2}[W_j^i - W_i][1 - W_i^\dagger W_j^i]^{-1}[1 - W_i^\dagger W_i]^{1/2} \quad j \geq i + 1 \tag{2.43}$$

Iterate through $i = 0, \ldots, n - 2$, we get all W_i.

The second stage of the algorithm is to solve $\Psi_n(z) \to \Psi_{n-1}(z) \cdots \to \Psi_0(z) = \Psi(z)$ where $\Psi(z), z \in \mathcal{D}$ is the final needed Schur interpolant. This is done by transcribing Eq. (2.41) and (2.42) as

$$V_i(z) = \frac{|z_i|(z_i - z)}{z_i(1 - z_i^\dagger z)}[I - W_i W_i^\dagger]^{1/2}\Psi_{i+1}(z)[I - W_i^\dagger W_i]^{-1/2} \tag{2.44}$$

$$\Psi_i(z) = [I + V_i(z)W_i^\dagger]^{-1}[V_i(z) + W_i] \tag{2.45}$$

with i iterating from $n - 1$ to 0.

Lastly, we get the Carathéodory interpolant to $F(z) = i\mathcal{G}(z)$ or $F(z) = i\Sigma(z)$ where $z \in \mathcal{C}^+$ by

$$F(z) = [I + \Psi(\frac{z - i}{z + i})]^{-1}[I - \Psi(\frac{z - i}{z + i})] \tag{2.46}$$

Stage one is done once, while stage two is called by Eq. 2.46 for each $z \in \mathcal{C}^+$ we want.

2.8   Demonstration for the Hubbard Dimer

We demonstrate the interpolation of the matrix-valued Green's function $\mathcal{G}(z)$, self-energy $\Sigma(z)$ and cumulant $M(z)$ of a Hubbard Dimer system, with the use of the above Carathéodory continuation algorithm.

With the creation operator $c_{i\sigma}^{\dagger}$ and annihilation operator $c_{i\sigma}$ obeying the fermion anticommutator relations, $\{c_{i\sigma}^{\dagger}, c_{j\sigma'}\} = \delta_{ij}\delta_{\sigma\sigma'}$ and $\{c_{i\sigma}, c_{j\sigma'}\} = \{c_{i\sigma}^{\dagger}, c_{j\sigma'}^{\dagger}\} = 0$, the number operator and double occupancy operator are defined as

$$n_{i\sigma} = c_{i\sigma}^{\dagger} c_{i\sigma} \tag{2.47}$$

$$D_i = n_{i\uparrow} n_{i\downarrow} \tag{2.48}$$

then the Hamiltonian of a Hubbard dimer system is

$$
\begin{aligned}
H_{sym} \quad &= H_0 + H_V & (2.49)\\
H_{asym} \quad &= H_0 + H_V + H_{\boldsymbol{H}} + H_{\text{breaksym}} & (2.50)\\
H_0 \quad &= -t\,(c_{0\uparrow}^{\dagger}c_{1\uparrow} + c_{0\downarrow}^{\dagger}c_{1\downarrow} + h.c.) - \mu\,(c_{0\uparrow}^{\dagger}c_{0\uparrow} + c_{1\uparrow}^{\dagger}c_{1\uparrow} + c_{0\downarrow}^{\dagger}c_{0\downarrow} + c_{1\downarrow}^{\dagger}c_{1\downarrow}) & (2.51)\\
H_V \quad &= U(D_0 + D_1) - U/2\,(n_{0\uparrow} + n_{1\uparrow} + n_{0\downarrow} + n_{1\downarrow}) & (2.52)\\
H_{\boldsymbol{H}} \quad &= \boldsymbol{H}\,(n_{0\uparrow} - n_{0\downarrow} + n_{1\uparrow} - n_{1\downarrow}) & (2.53)\\
H_{\text{breaksym}} \quad &= U_a(D_0 - D_1) + \mu_a(n_{0\uparrow} + n_{0\downarrow} - n_{1\uparrow} - n_{1\downarrow}) + \boldsymbol{H}_a(n_{0\uparrow} - n_{0\downarrow} - n_{1\uparrow} + n_{1\downarrow}) & (2.54)
\end{aligned}
$$

Here we use the degeneracy-lifted Hamiltonian $H = H_{asym}$ with parameters $\beta = 10$, $t = 1$, $U = 5$, $\mu = 0.7$, $\boldsymbol{H} = 0.3$, $U_a = 0.5$, $\mu_a = 0.2$, $\boldsymbol{H}_a = 0.03$.

Results are shown in Fig. 2.2. We interpolated 4×4 matix-valued [2×2-orbital (both spin up and spin down) dimer system] Green's, self-energy and cumulant response functions. Imaginary lines show exact data on the real axis calculated by the analytic model formula. Real lines show the results of continuing matrices as a whole (not seperated by entries) from the imaginary axis to the real axis (input analytic data are disturbed by 10^{-7} standard deviation Gaussian random noise). It is clearly shown that the Carathéodory continuation theory works perfectly for our analytic dimer data, both ensuring causality and providing unprecedented resolution. More exciting trials on real systems are still in progress.
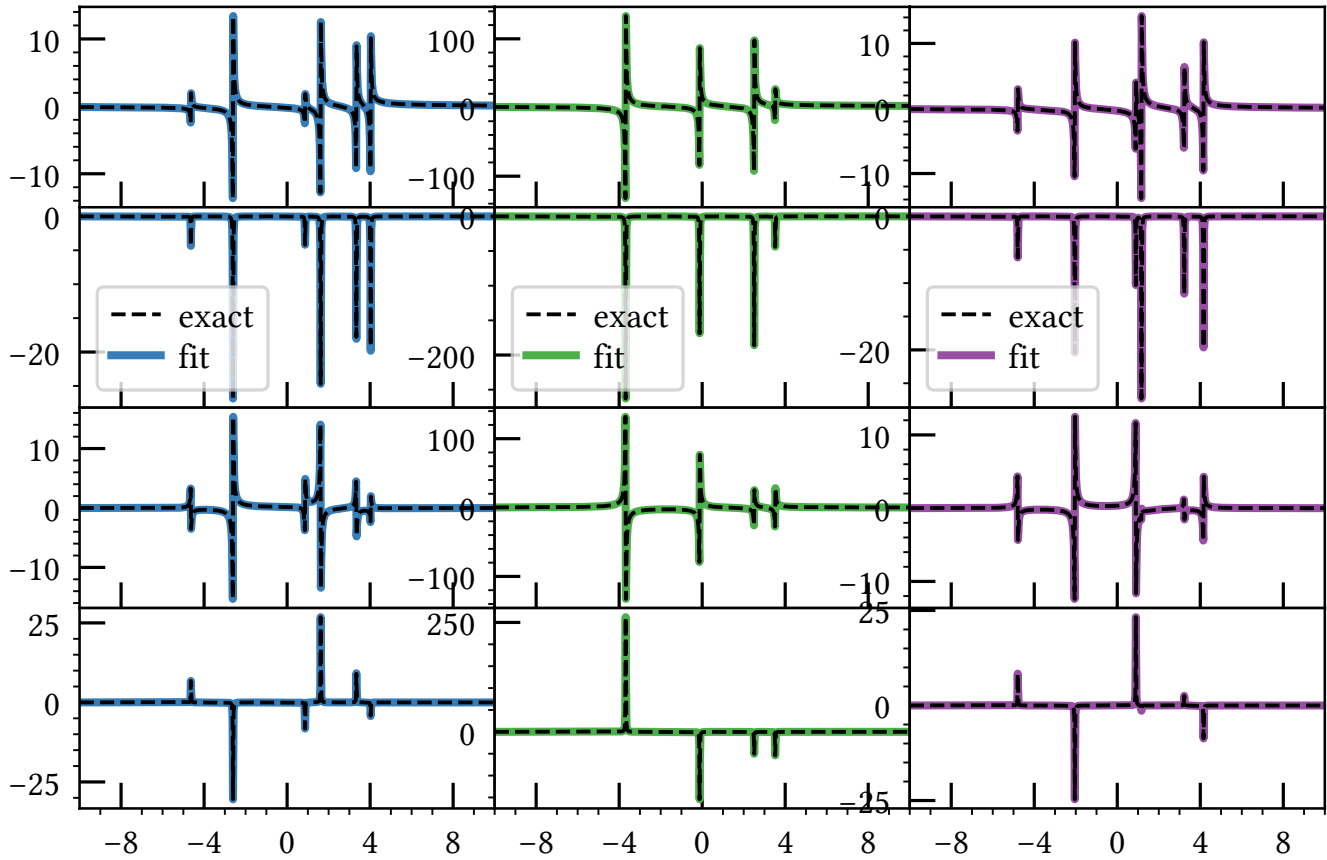
Figure 2.2: The Hubbard dimer model interpolation, 2 random non-zero entries [rows are real(1), imaginary(1), real(2), imaginary(2) part] of the 4×4 matrices, on the real axis. Using input data with 10^{-7} standard deviation Gaussian noise. Left are Green's functions, middle are self-energies, right are cumulants. The exact data comes from analytic model formula. Fitted data comes from continuing matrices from the imaginary axis, which we get from analytic formula and disturbed with noise.

Chapter 3

Perovskite Oxides Physics

3.1 Properties of $SrTiO_3$

The transition metal oxides that crystallize in perovskite structure has long been the study subject, because they exhibit a wide range of exotic structural, electronic and magnetic behaviors, and show importance in several areas of technology. We study the spectral property of strontium titanate ($SrTiO_3$) in this work, which is the simplest cubic perovskite oxides while the foundation of the emerging field of oxide electronics [33].

Pure $SrTiO_3$ crystal is a paraelectric in which quantum fluctuations persist to zero temperature and prevent the emergence of long-range order. However, it shows proximity to a ferroelectric phase, suggested by a large rise in dielectric susceptibility and the softening of polar mode F_{1u} upon cooling, and referred to as incipient ferroelctric [34]. Ferroelectricity, the spontaneous electric polarization owned by materials, is crucial to applications such as tunable capacitor, ferroelectric RAM, etc. Experiments further demonstrated various ways to realize a ferroelectric phase transition for $SrTiO_3$, by intrinsic ^{18}O isotope [35], electric field [36], biaxial stress [37], optical strain [34], dopant (Ca) substitution and so on.

Besides incipient ferroelectricity, the structural phase transition of $SrTiO_3$ (F_{2u} phonon mode condensation) from cubic to tetragonal at $T_c = 105K$ is another focus. Free energy formulation connects the dielectric and strutural quadratic term to stress and show their mutual interaction [38] (See Fig. 3.1 for diagram). In addition, exotic properties of $SrTiO_3$ heterostructures with other perovskite and 2D materials is a growing area of research. $FeSe - SrTiO_3$ interface displays over 100 K high-Tc superconductivity [39, 40]; $SrTiO_3 - LaMnO_3$ interface displays colossal magnetoresistance [41], $SrTiO_3 - LaAlO_3$ interface displays combinations of novel electric and magnetic phenomena. Other useful properties of strontium titanate include photovoltaic effect [42], water photolysis, blue-light emission and so on.

Proper understanding of these properties requires the knowledge of the bulk material electronic structure. At room temperature $SrTiO_3$ unit cell is in the ABC_3 undistorted cubic structure with a 3.905 Å lattice constant (See Fig. 3.1). Perfect $SrTiO_3$ crystal is an insulator due to the d^0 configuration of the titanium ion, with an experimentally determined indirect band gap of 3.25 eV and direct gap of 3.75 eV [43]. Crystal field further splits the fivefold-degenerate unoccupied d levels into t_{2g} and e_g subgroups, octahedral symmetry makes t_{2g} levels lower than e_g levels for Ti, and vice versa for dodecahedral symmetric Sr [44]. In a more detailed classification, the upper valence band has 18 electrons in total originating from six 2p electrons per oxygen atom. The lower valence band is filled with 12 electrons including six oxygen 2s and six Sr 4p electrons. Semicore level electron states involve two Sr 4s, six Ti 3p and 2 Ti 3s electrons [44, 45].
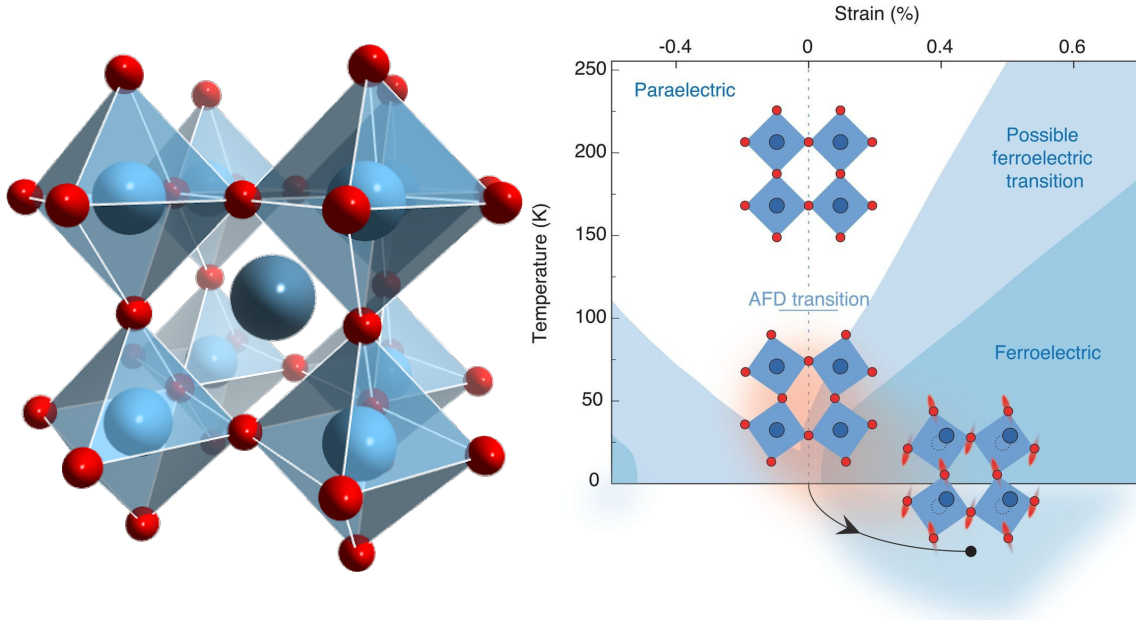
Figure 3.1: Left: Cubic perovskite unit cell. TiO_6 octahedra and central Sr cation as for $SrTiO_3$. Right: Structural phase diagram of $SrTiO_3$ [34].

3.2 GW Approximation

The $SrTiO_3$ solid is modeled as an arrangement of atoms in a three dimension Bravais lattice. We use the Bloch waves constructed from Gaussian basis as the single-particle wave functions,

$$\phi_{\mathbf{k}_i,i}(\mathbf{r}) = \sum_{\mathbf{R}} \phi_i^{\mathbf{R}}(\mathbf{r}) e^{i\mathbf{k}\cdot\mathbf{R}} \tag{3.1}$$

where $\phi_i^{\mathbf{R}}(\mathbf{r})$ is the localized atomic orbital centered in Bravais lattice cell $\mathbf{R}$. These non-orthogonal states define the overlap matrix,

$$\mathbf{s}_{ij} = \int_{\Omega} d\mathbf{r} \phi_i^*(\mathbf{r}) \phi_j(\mathbf{r}) \delta_{\mathbf{k}_i,\mathbf{k}_j} \tag{3.2}$$

and we use the combined orbital-momenta index $\boldsymbol{i} = (i, \mathbf{k}_i)$ from now on.

The electronic structure Hamiltonian in second quantization is

$$H = \sum_{\boldsymbol{ij}} h_{ij}^0 c_i^\dagger c_j + \frac{1}{2} \sum_{\boldsymbol{ijkl}} v_{ijkl} c_i^\dagger c_k^\dagger c_l c_j \tag{3.3}$$

where c_i ($c_i^\dagger$) are annihilation (creation) operators corresponding to the single particle state $\phi_i(\mathbf{r})$. The single-particle operator h_{ij}^0 and two-particle operator v_{ijkl} are defined respectively as

$$h_{ij}^0 = \int_\Omega d\mathbf{r} \phi_i^*(\mathbf{r}) \left[-\frac{1}{2}\nabla_\mathbf{r}^2 - \sum_\alpha \frac{Z_\alpha}{r_{\alpha,\mathbf{r}}} \right] \phi_j(\mathbf{r}) \tag{3.4a}$$

$$v_{ijkl} = \frac{1}{V} \int_\Omega d\mathbf{r} \int_{\mathbb{R}^3} d\mathbf{r}' \frac{\phi_i^*(\mathbf{r})\phi_j(\mathbf{r})\phi_k^*(\mathbf{r}')\phi_l(\mathbf{r}')}{|\mathbf{r}-\mathbf{r}'|} \tag{3.4b}$$

where Z_α is the nuclear charge of atom α, $r_{\alpha,\mathbf{r}} = |\mathbf{r} - \mathbf{r}_\alpha|$ is the distance to nucleus α at r_α, Ω is the volume of the unit cell and V is the volume of the system.

We investigate the single-particle spectral functions $A_{ij}^\mathbf{k}(\omega)$ in this work. The local ones are defined by $A_{ii}(\omega) = \frac{1}{N_\mathbf{k}} \sum_k A_{ii}^\mathbf{k}(\omega)$ where N_k is the total number of k points in the first Brillion zone, while the k-resolved ones are given by $A^\mathbf{k}(\omega) = \sum_i A_{ii}^\mathbf{k}(\omega)$.

Our central object is therefore the Green's function whose diagonal element imaginary part carries the single-particle spectra information. Imaginary-time Green's function is defined as,

$$G_{ij}^\mathcal{H}(\tau) = -\frac{1}{\mathcal{Z}} Tr \left[e^{-(\beta-\tau)(\mathcal{H}-\mu N)} c_i e^{-\tau(\mathcal{H}-\mu N)} c_j^\dagger \right] \tag{3.5}$$

where we use the grand canonical ensemble, μ is the chemical potential and N is the total particle number. Denote non-interacting Green's function as $G_{ij}^0(\tau) = G_{ij}^{H^0}(\tau)$, where $H^0 = \sum_{ij} h_{ij}^0 c_i^\dagger c_j$, and the interacting one as $G_{ij}(\tau) = G_{ij}^H(\tau)$. Note that Green's function is diagonal in momenta space because of the lattice translational invariance.

Dyson equation then gives the definition of the self-energy,

$$\Sigma_{ij}(\tau) = \left(G_{ij}^0(\tau) \right)^{-1} - \left(G_{ij}(\tau) \right)^{-1} \tag{3.6}$$

whose physical meaning can be interpreted as the effective one-body potential describing one particle's interaction with the rest of the system.

Before going into GW algorithm, let's further introduce a technique utilized in our group's code, the Cholesky Coulomb integral decomposition which avoids to store the 4-index tensor and makes the algorithm practical [46]. See the diagram in Fig. 3.2 left panel. We decompose the interaction as $v_{i_1 i_2 i_3 i_4} = V_{i_1 i_2}^Q V_{i_3 i_4}^Q$ where Q is an auxiliary index and $V_{i_1 i_2}^Q$ is a three-point integral defined as

$$V_{i_1 i_2}^Q = \sum_P \int_\Omega d\mathbf{r}d\mathbf{r}' \frac{\phi_{i_1}^*(\mathbf{r})\phi_{i_2}(\mathbf{r})\chi_P^\mathbf{q}(\mathbf{r}')}{|\mathbf{r}-\mathbf{r}'|} J^{-\frac{1}{2}\mathbf{q}}_{PQ} \tag{3.7}$$

with momentum transfer $\mathbf{q} = \mathbf{k}_{i_1} - \mathbf{k}_{i_2} = \mathbf{k}_{i_3} - \mathbf{k}_{i_4}$, $\chi_P^\mathbf{q}(\mathbf{r}')$ an auxiliary basis function and $\mathbf{J}^{-1} = \mathbf{J}^{-\frac{1}{2}}\mathbf{J}^{-\frac{1}{2}}$ the inverse of

$$J_{PQ}^\mathbf{q} = \int_\Omega d\mathbf{r}d\mathbf{r}' \frac{\chi_P^{\mathbf{q}*}(\mathbf{r})\chi_Q^\mathbf{q}(\mathbf{r}')}{|\mathbf{r}-\mathbf{r}'|} \tag{3.8}$$

Storing the integrals V_{ij}^Q beforehand is therefore affordable and would greatly enhance the GW algorithm efficiency.

3.2.1 Ground State Starting Point

In the Feynman diagram language, the non-interacting bare propagator $G_{ij}^0(\tau)$ could take in the self-energy $\Sigma_{ij}(\tau)$ which involves the many-body effects, and be turned into a 'dressed' propagator $G_{ij}(\tau)$. The Matsubara (imaginary) frequency formalism is introduced for convenience to relate $G(\omega_n)$ and $\Sigma(\omega_n)$, as

$$G(\omega_n) = \left[(\omega_n + \mu)\mathbb{1} - H^0 - \Sigma(\omega_n) \right]^{-1} \tag{3.9}$$

Therefore, to get the total Green's function, we need the total self-energy of the system, which has the diagrammatic expansion of all one-particle irreducible diagrams, with zeroth order to infinite order interactions. Practical calculations should add up only a subclass of all diagrams, which is either truncated in order or have topological similarity that enables resummation.

The zeroth and first order interactions are static with no frequency dependence (no propagator crossing through different τs), and is conventionally called mean-field interaction (average force on one particle). Despite the low cost of mean-field theory calculations, we need higher-order self-energy diagrams to count for the higher-level correlations for solids who have moderate to strong correlations, like $SrTiO_3$. But we start with a ground state mean-field theory calculation, the local density approximation (LDA), to give a reasonable initial guess of the self-energy $\Sigma_{\infty,ij}(\omega)$.

The matrix element of the Fock matrix, i.e., the zeroth and first order self-energy, is defined as,

$$\mathcal{F}_{ij} = h_{ij}^0 + \Sigma_{\infty,ij} = h_{ij}^0 + \sum_{kl} \rho_{lk}(v_{ijkl} - \frac{1}{2}v_{ilkj}) \tag{3.10}$$

including a direct and an exchange term. ρ is the density matrix of the system which is often stored in the k-resolved form and should reach self-consistency together with $\mathcal{F}$.

The aim of the LDA calculation is to give us the explicit ground state Fock matrix, as well as the non-interacting Hamiltonian H_0, overlap matrix **s**, Coulomb interaction decoupled three-index integrals $V_{i_1 i_2}^Q$, by the use of python package PySCF [47] which saves us time and effort.

3.2.2 Self-Consistent GW (scGW)

Hedin's finite temperature GW approximation is a generalization of Hartree Fock (HF) approximation, which replaces the bare interaction exchange diagram with an RPA-like vertex function. This interaction is dynamic (frequency resolved) and renormalized, therefore reflects the dynamically screened interaction similar to the physical screening every electron is feeling from its surrounding moving medium. There are many variants of GW including the second order perturbation theory (GF2) [48, 49], quasi-particle self-consistent GW (QSGW) [50], etc. In this work, the self-consistent GW (scGW) is applied as the weakly-correlated level of approximation [19, 46].

scGW is thermodynamically conserving and consistent. It is so called 'GW' because the approximate GW self-energy (beyond the Fock matrix) contains both a dressed propagator G and
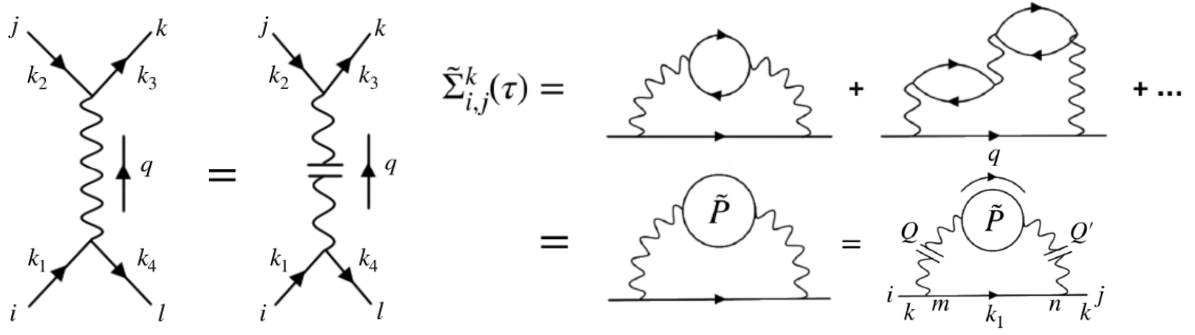
Figure 3.2: Left: Cholesky decouple of Coulomb interaction. Right: Diagrams beyond the Hartree diagram in the scGW approximation, using interaction decomposition.

the 'screened iteraction' term $\tilde{W}$ [51]. $\tilde{W}$ can be expanded diagrammatically in the RPA ring-diagram series as shown in the Fig. 3.2 right panel (upper arc). Or the $\tilde{W}_{i\,j\,k\,l}^{\mathbf{k}_1\mathbf{k}_2\mathbf{k}_3\mathbf{k}_4}$ can be expanded mathematically as

$$\tilde{W}_{ijkl}(\tau) = \frac{-1}{N_k}\{V_{il}^Q \tilde{P}_{0,Q,Q'}^{\mathbf{q}}(\tau)V_{jk}^{Q'} + \int_0^\beta d\tau' V_{il}^Q \tilde{P}_{0,Q,Q'}^{\mathbf{q}}(\tau')\tilde{P}_{0,Q',Q''}^{\mathbf{q}}(\tau-\tau')V_{jk}^{Q''} + ...\} \tag{3.11}$$

with momentum transfer $\mathbf{q} = \mathbf{k}_1 - \mathbf{k}_4 = \mathbf{k}_3 - \mathbf{k}_2$ and

$$\tilde{P}_{0,Q,Q'}^{\mathbf{q}}(\tau) = \frac{2}{N_k}V_{p\,m}^{Q,\mathbf{k},\mathbf{k}+\mathbf{q}}G_{tp}^{\mathbf{k}}(-\tau)G_{mn}^{\mathbf{k}+\mathbf{q}}(\tau)V_{n\,t}^{Q',\mathbf{k}+\mathbf{q},\mathbf{k}} \tag{3.12}$$

where repeated indices are summed over.

The convolutions in Eqn. 3.11 can be circumvented within the Matsubra frequency domain in terms of an infinite geometrical series. Define

$$\tilde{P}^{\mathbf{q}}(i\Omega_n) = \sum_{t=1}^\infty [\tilde{P}_0^{\mathbf{q}}(i\Omega_n)]^t = [I_Q - \tilde{P}_0^{\mathbf{q}}(i\Omega_n)]^{-1}\tilde{P}_0^{\mathbf{q}}(i\Omega_n) \tag{3.13}$$

where $i\Omega_n = \frac{2n\pi}{\beta}$ ($n = 0, \pm 1, ...$), then each element in Eqn. 3.13 is a $Q \times Q$ square matrix. We transform $\tilde{P}^{\mathbf{q}}$ back to the imaginary-time domain using Chebyshev convolution tricks, which gives us the expression for screened interaction

$$\tilde{W}_{ijkl}(\tau) = \frac{-1}{N_k}V_{i\,l}^{Q,\mathbf{k}_1\mathbf{k}_4} \tilde{P}_{Q,Q'}^{\mathbf{q}}(\tau)V_{j\,k}^{Q',\mathbf{k}_2\mathbf{k}_3} \tag{3.14}$$

The supplemented GW self-energy is

$$\begin{aligned}
\tilde{\Sigma}_{ij}^{\mathbf{k}}(\tau) &= G_{m,n}^{\mathbf{k}_1}(\tau)\tilde{W}_{i\,n\,j\,m}^{\mathbf{k},\mathbf{k}_1,\mathbf{k},\mathbf{k}_1}(\tau) \\
&= \frac{-1}{N_k}V_{i,m}^{Q,\mathbf{k},\mathbf{k}_1}G_{m,n}^{\mathbf{k}_1}(\tau)\tilde{P}_{Q,Q'}^{\mathbf{q}}(\tau)V_{n,\,j}^{Q',\mathbf{k}_1,\mathbf{k}}
\end{aligned} \tag{3.15}$$

with $\mathbf{q} = \mathbf{k} - \mathbf{k}_1$, or diagrammatically as shown in the Fig. 3.2 right panel. Finally, the total self-energy $(\Sigma^{GW})_{ij}^{\mathbf{k}}(\tau) = \mathcal{F}_{ij} + \tilde{\Sigma}_{ij}^{\mathbf{k}}(\tau)$, while the new Green's function is obtained by Eqn. 3.9 (calculated in the Matsubara frequency domain).
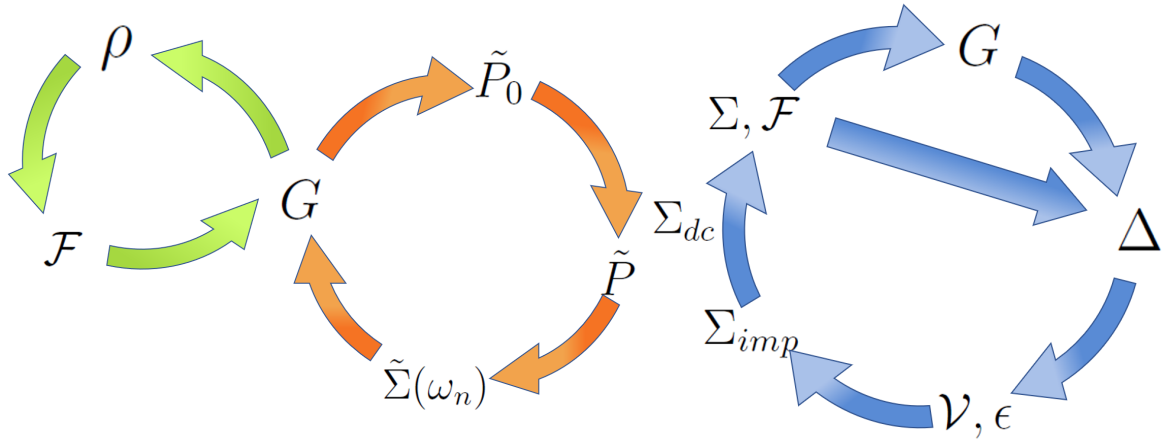
Figure 3.3: Left: scGW self-consistency loop. Firstly $\rho \to \mathcal{F}$, secondly $G \to \tilde{\Sigma}(\omega_n)$, thirdly calculate G, finally update density matrix ρ. Right: SEET inner loop, starting from $\Sigma, \mathcal{F}$, with Σ_{imp} solved by ED impurity solver. scSEET connects one-shot GW to one-shot inner loop with the $G, \mathcal{F}$ and Σ, iterating until $\mathcal{F}, \Sigma$ reach convergence.

I show the above procedure in the right loop of Fig. 3.3 left panel. The left loop starts by updating the Fock matrix $\mathcal{F}$ by density matrix ρ using Eqn. 3.10. After G is provided in the right loop, ρ is renewed as $\rho = -2G(\beta)$.

3.3 Self-Energy Embedding Theory (SEET)

3.3.1 Inner loop for Impurity Problem

As the next step, we want to take the correlation which is stronger than the mean-field and the screened interaction into effect. We rely on a Φ-derivable quantum embedding theory, the so-called self-energy embedding theory (SEET) [19, 46], which is thermodynamically consistent and obeys the conservation law. In this theory, we supplement the long-range GW screening with the selected local strongly-correlated subspaces. The subspace self-energy is obtained by an exact diagonalization (ED) quantum impurity solver and fed back to the total self-energy iteratively until convergence. The workflow is shown in the Fig. 3.3 right panel.

The core here is one equation, which non-perturbatively adds local strong interaction diagrams to the GW self-energy, and removes the double-counting terms

$$\Sigma_{ij}^{\mathbf{k}} = (\Sigma^{GW})_{ij}^{\mathbf{k}} + \sum_A \left((\Sigma_A^{\text{imp}})_{ij} - (\Sigma_A^{\text{DC-GW}})_{ij} \right) \delta_{(ij)\in A} \tag{3.16}$$

also can be Fourier transformed to real space as

$$\Sigma_{ij}^{\mathbf{RR'}} = (\Sigma^{GW})_{ij}^{\mathbf{RR'}} + \sum_A \left((\Sigma_A^{\text{imp}})_{ij} - \Sigma_A^{\text{DC}})_{ij} \right) \delta_{\mathbf{RR'}} \delta_{(ij)\in A} \tag{3.17}$$

each Σ here includes the first order term Σ_∞ and the frequency dependent part $\Sigma(\omega_n)$, e.g., $\Sigma^{\text{imp}} = \Sigma_\infty^{\text{imp}} + \Sigma^{\text{imp}}(\omega_n)$.

Subsets A of impurity orbitals with indices $ij \in A$, sometimes also called active orbitals, are defined as groups of the most physically relevant orbitals for the problem that have correlations

that are necessary to be included at a higher than perturbative level. Double counting terms are the GW diagrams that have both external legs i and j in the active space but contain one or more internal indices on the remaining orbitals.

We next come to the SEET embedding condition

$$(G(\omega_n))_{ij \in A}^{\mathbf{RR}} = \left[(\omega_n + \mu)\mathbb{1} - h_{ij \in A}^{0,\mathbf{RR}} - \Sigma_{ij \in A}^{\mathbf{RR}} - \Delta_{ij}^A(\omega_n) \right]^{-1} \quad (3.18)$$

here the hybridization matrix $\Delta_{ij}^A(\omega_n)$ arises because of the algebra when inverting the matrix $(G(\omega_n))^{\mathbf{RR}}$ and taking its subset (not the same as the inverse of a subset). Δ_{ij}^A is calculated from $G^{\mathbf{RR}}$ and $\Sigma^{\mathbf{RR}}$ in the present iteration and taken as the mean-field bath for the impurity model, commonly the Anderson impurity model

$$H_{\mathrm{And}} = H_0 + \sum_{\gamma} \epsilon_{\gamma}^{\mathrm{bath}} n_{\gamma}^{\mathrm{bath}} + \sum_{\gamma} (\mathcal{V}_{\gamma} c_0^{\dagger} a_{\gamma}^{\mathrm{bath}} + h.c.) \quad (3.19)$$

where $c_0^{\dagger}$ creates an atomic electron and $a_{\gamma}^{\mathrm{bath}}$ annihilates a bath electrons. Bath parameters $\mathcal{V}$ and ϵ are optimized by minimizing the fit residue

$$\chi_i^2 = \sum_n f(n) \| \Delta_{ii}(\omega_n) - \sum_{b=1}^{N_b} \frac{\mathcal{V}_{ib} \mathcal{V}_{ib}^*}{i\omega_n - \epsilon_b} \|, \quad (3.20)$$

where n is the number of orbitals in an impurity, N_b is the number of bath orbitals corresponding to one atomic orbital, $f(n)$ is chosen to suppress high frequency contributions to $\Delta_{ii}(\omega_n)$ (we usually choose $f(n) = 1/\omega_n$).

We then just solve H_{And} with an ED solver. Finally, after exponential scaled impurity solving, we get the impurity self-energy Σ^{imp} and calculate the next Σ, G from Eqn. 3.16 and 3.9 (getting rid of Σ_{DC}). We loop until self-consistency in the right loop of Fig. 3.3 is achieved. This method is free from any semi-empirical adjustable parameters.

3.3.2 'One-shot GW + One-shot Inner-loop' Iteration as Outer Loop

The outer-loop scSEET combines 'one-shot GW' with 'one-shot inner-loop' by an iterative pipeline between the two jobs, where we take the self-energy matrix Σ, Green's function matrix G and Fock matrix $\mathcal{F}$ as output from one job and feed it as input to the other, as shown in Fig. 3.3. The idea of this procedure is that we take bare interaction as input, then each iteration 'inserts' diagram into the self-energy. For example, when we take the partially boldified propagator G out from SEET and into GW, the local strong correlation in the diagrams is supplemented by some non-local diagrams from GW. The insertion of strong-correlation is one form of 'vertex correction' for GW. When we reach self-consistency (defined on the convergence of Σ and $\mathcal{F}$ with the period of a full outer-loop), the propagator G is fully boldified. Outer-loop gives more in-time balance and stability than the mere inner-loop as this work will demonstrate.

3.4 Results

A number of photoemission (PES) and inverse photoemission spectroscopy (IPES) experiments have investigated the spectral function of $SrTiO_3$ [52–55]. We compare our calculated spectral functions with the experimental XPS (x-ray photoemission spectroscopy) and IPES data from

Ref. [54, 55]. The relative height between XPS and IPES spectra was arbitrary. The band-gap was defined as between the 'intercept of the valence band right-most feature linear fit upon the x-axis' and the 'bottom of the conduction band' [52], which was generally recognized as 3.2 eV locally in the lattice. Experimental error of the XPS data we used was ± 0.8 eV in frequency [55].

First, computational details necessary for reproducing our calculation are listed here. Hamiltonian is solved with Gaussian *gth-dzvp-molopt-sr* basis [17] and *gth-pbe* pseudopotential [18]. The Coulomb integrals are decomposed into the tempered Gaussian for *Sr* and *def2-svp-ri* bases [24] for all other atoms. Integrals are obtained from the open source PySCF package [47]. The inverse temperature used throughout this work is $\beta = 300 Ha^{-1}$ (T $\sim$ 1053 K $\sim$ 0.09 eV). SEET setup has 3 bath / orbital for 3-orbital impurity, 5 bath / orbital for 2-orbital impurity.

3.4.1 GW Approximation

Fig. 3.4 shows results from the self-consistent GW calculation. Top and bottom panel respectively shows the local total density of states of $SrTiO_3$ and the orbitally resolved spectral functions for the near-Fermi orbitals. As expected, the top of the valence band is dominant by O 2p states, while the bottom of the conduction band by Ti 3d states.

In scGW, our calculated spectra has a deviation of the zero energy from the experimental data. An upward shift of about 1.5 *eV* of the experimental data could overlap them roughly in shape. There are two possible causes. First is due to the n-type dopants in experiments. Most of the electron spectroscopic measurements lightly doped $SrTiO_3$ with Nb^{5+} or La^{3+} cations to avoid the charging effect which typically happened [52]. This caused a slight lift of the Fermi energy of about 0.35 eV (compared to the average of p- and n-type) [53]. The second reason may be the electron attribution (chemical potential corresponded to the electron number, and all electrons embedded below Fermi level) during our GW calculation. Because $SrTiO_3$ is a wide-gap insulator, there may be a remaining freedom in choosing Fermi energy both in the k-space and in the real space.

Except the spectra shift and too-wide bandgap, our analytically continued spectra matched well in the orbital order (both total DOS and orbitally-resolved) with the experiment. The $4 \times 4 \times 4$ to $6 \times 6 \times 6$ convergence showed $6 \times 6 \times 6$ was a good size of k-grid to go on. We have checked that the main features from Maxent analytic continuation were consistent with both Nevanlinna and Padé continuation, except that Maxent suffered from resolution while Nevanlinna and Padé suffered from the input precision (convergence $\triangle E = 1e-5$ Ha) and showed some extent of artificial oscillations.

3.4.2 SEET Method

Inner loop

Name	Imp	Description
A	1	Ti t_{2g}
B	3	Ti t_{2g}; O p_π; O p_σ
C	4	Ti t_{2g}; Ti e_g; O p_π; O p_σ

Table 3.1: Choice of the SEET inner-loop active space for $SrTiO_3$. Imp denotes the number of distinct disjoint impurity problems.
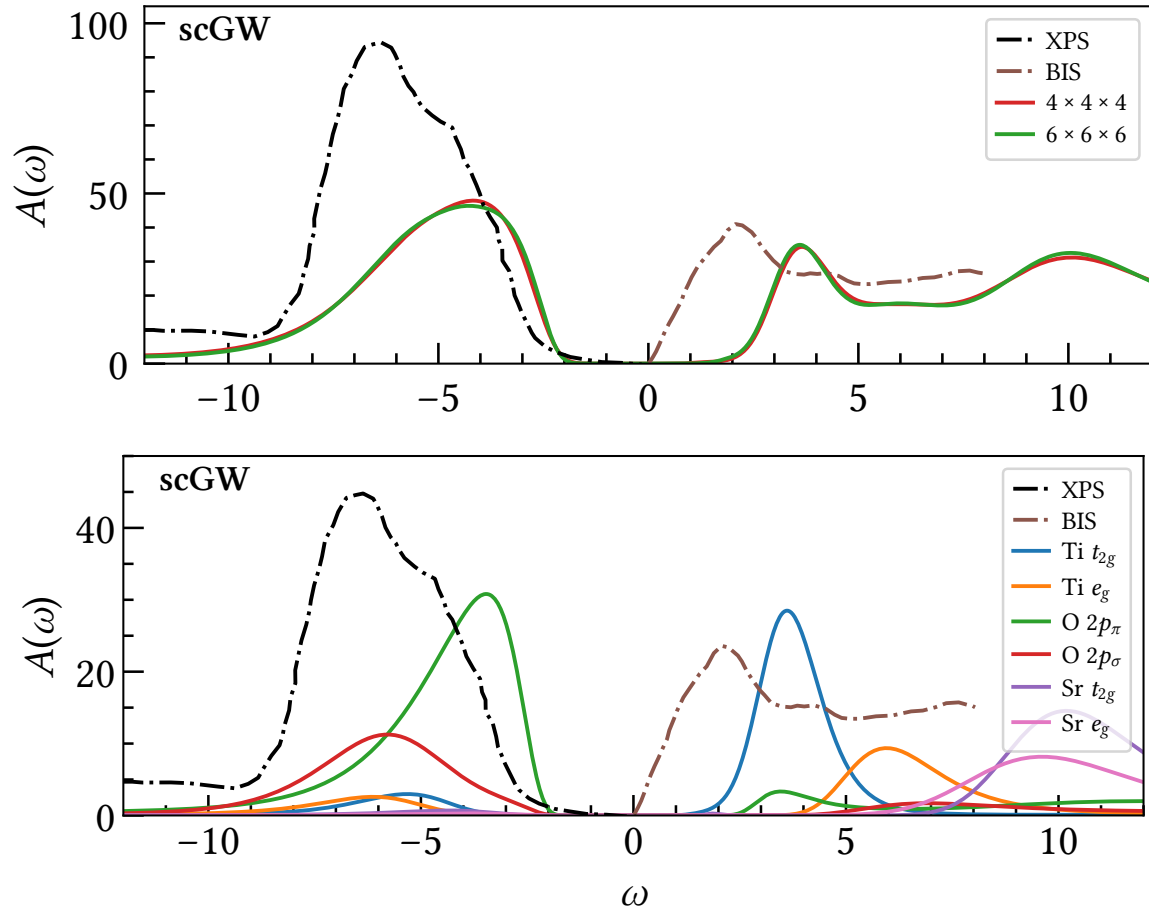
Figure 3.4: Top panel: Local total DOS of $SrTiO_3$ from scGW. Bottom panel: Local orbitally resolved DOS for $SrTiO_3$. Experimental XPS and IPES data from Ref. [54, 55].

In the simple ionic model, $SrTiO_3$ does not have Ti 3d electrons and thus have no appreciable correlation effects. However, Ti 3d orbitals hybridize strongly with O 2p orbitals, which have in experiments led to non-vanishing 3d electrons in the ground state and the interesting 'charge-transfer' satellite peaks in the valence band core levels [53].

The 'charge-transfer' peaks are high-energy features. Humps were vaguely observed by 'SEET + Nevanlinna' though we could not take them for sure. The $p - d$ hybridization between O and Ti states was well-demonstrated all through our calculation. As shown by the peak-position correspondence, Ti e_g state coupled strongly with O p_π state (bonding MO), while t_{2g} with p_σ state (non-bonding MO). This can be explained by the crystal symmetry. O 2p orbitals extend along the Cartesian axes, therefore one can expect large spatial overlap of p_z with d_{z^2} and $p_{x,y}$ with $d_{x^2-y^2}$ orbitals giving rise to $e_g - p_\pi$ hybridization [44].

Let's consider the effect of adding disjoint Ti t_{2g}, O p and Ti e_{2g} impurity subspace one-by-one using the inner-loop SEET calculation. Fig. 3.5 top panel resulted from the Ti t_{2g} impurity (3 orbitals). Valence band t_{2g} density was obviously increased while conduction band t_{2g} density was decreased compared to GW solution. Noticeably, the O p_σ peak increased in height substantially and became much sharper.

In Fig. 3.5 setup B, we added in the O 2p subspace (one p_π and one p_σ impurity) and included

the other two oxygen atom p orbitals non-perturbatively by symmetry. Again it were the Ti t_{2g} and O p_σ states that responded with their great enhancement. Both A and B setups showed that t_{2g} and p_σ were interacting strongly through the formalism of Dyson equation. Finally, we placed the Ti e_g impurity (2 orbitals, Fig. 3.5 bottom panel). The only visible change was a slight increase in width of the e_g feature in the conduction band, showing the broadening effect which may due to the high-level correlation.

Outer loop

Name	Imp	Description
A	1	Ti t_{2g}
B	3	Ti t_{2g}; O p_π; O p_σ
C	4	Ti t_{2g}; Ti e_g; O p_π; O p_σ
D	3	Ti t_{2g}; Ti $d_{x^2+y^2}$ + O p_x, p_y; Ti d_{z^2} + O p_z

Table 3.2: Choice of the SEET outer-loop active space for $SrTiO_3$. Imp denotes the number of distinct disjoint impurity problems.

The outer-loop (fully self-consistent) SEET combined the one-shot GW and one-shot SEET, which created two effects compared to the inner-loop SEET. The first was that the sharp quasiparticle peak at the Fermi energy disappeared (exhibited in the Ti t_{2g} orbitals). The second was that the near-Fermi orbitals (Ti t_{2g}, Ti e_g, O $2p_\sigma$, O $2p_\pi$) had shifted right for about 1 eV with respect to the inner-loop spectra. These effects probably lied in the deficiency of the inner-loop calculation, because it lacked the GW non-local feedback to the strongly-correlated subspace. Similar redundant oscillation also occurred in the $SrVO_3$ simulation of our group's (Ref. [19] Appendix E).

We also note the lowered O $2p_\pi$ density. Since the relative peak heights of XPS and BIS data were arbitrary, there was no evidence that either inner-loop or outer-loop was less accurate.

3.4.3 Summary

Finally, let's see Fig. 3.7 which demonstrated the development of local total density of state from the initial guess of an LDA solution to scGW to inner-loop and outer-loop SEET. We mention two significance.

First was the spectra shift and bandgap narrowing which drove the system closer and closer to experimental data. Bandgap was experiencing the change of 4.2 eV (LDA), 3.8 eV (GW), 2.9 eV (inner-loop SEET A), 3.3 eV (inner-loop SEET B and C), 2.8 eV (outer-loop SEET A and B) to 3.3 eV (outer-loop SEET C), which perfectly matched experimental determined gap. Second was that the Fermi level was moving towards the correct position all the way till outer-loop SEET setup C, despite the detour of the inner-loop SEET since the artificial oscillations had obscured its accomplishment on the correct zero energy position. Last but not least, the final shape of the $SrTiO_3$ single-particle excitation spectrum much resembled the experiments, proving a systematic improvement throughout the whole scSEET process.
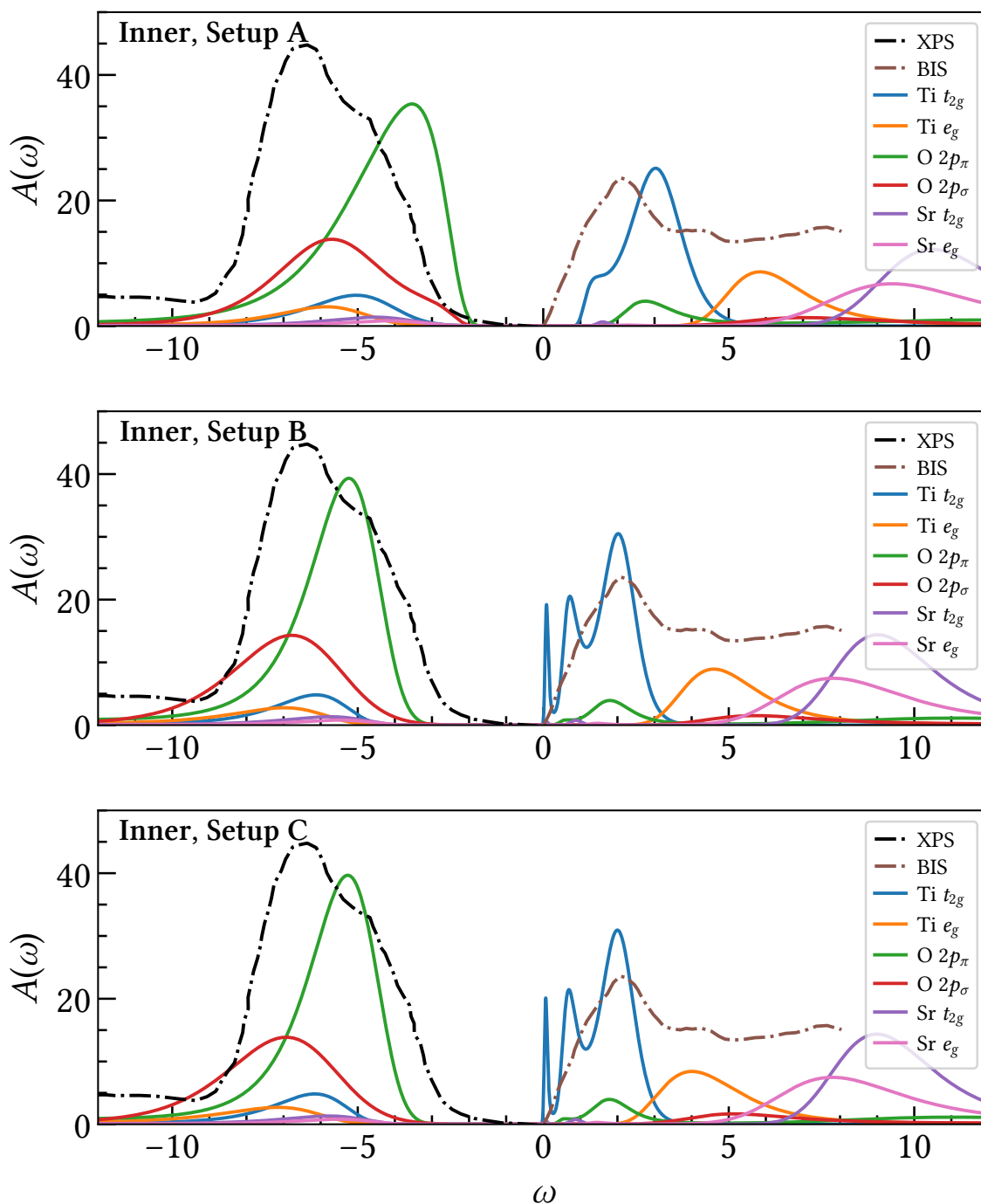
Figure 3.5: SEET inner-loop local orbitally resolved spectral functions for setup A (Ti t_{2g}), B (Ti t_{2g}; O p_π; O p_σ), C (Ti t_{2g}; Ti e_g; O p_π; O p_σ). Experimental XPS and IPES data from Ref. [54, 55].
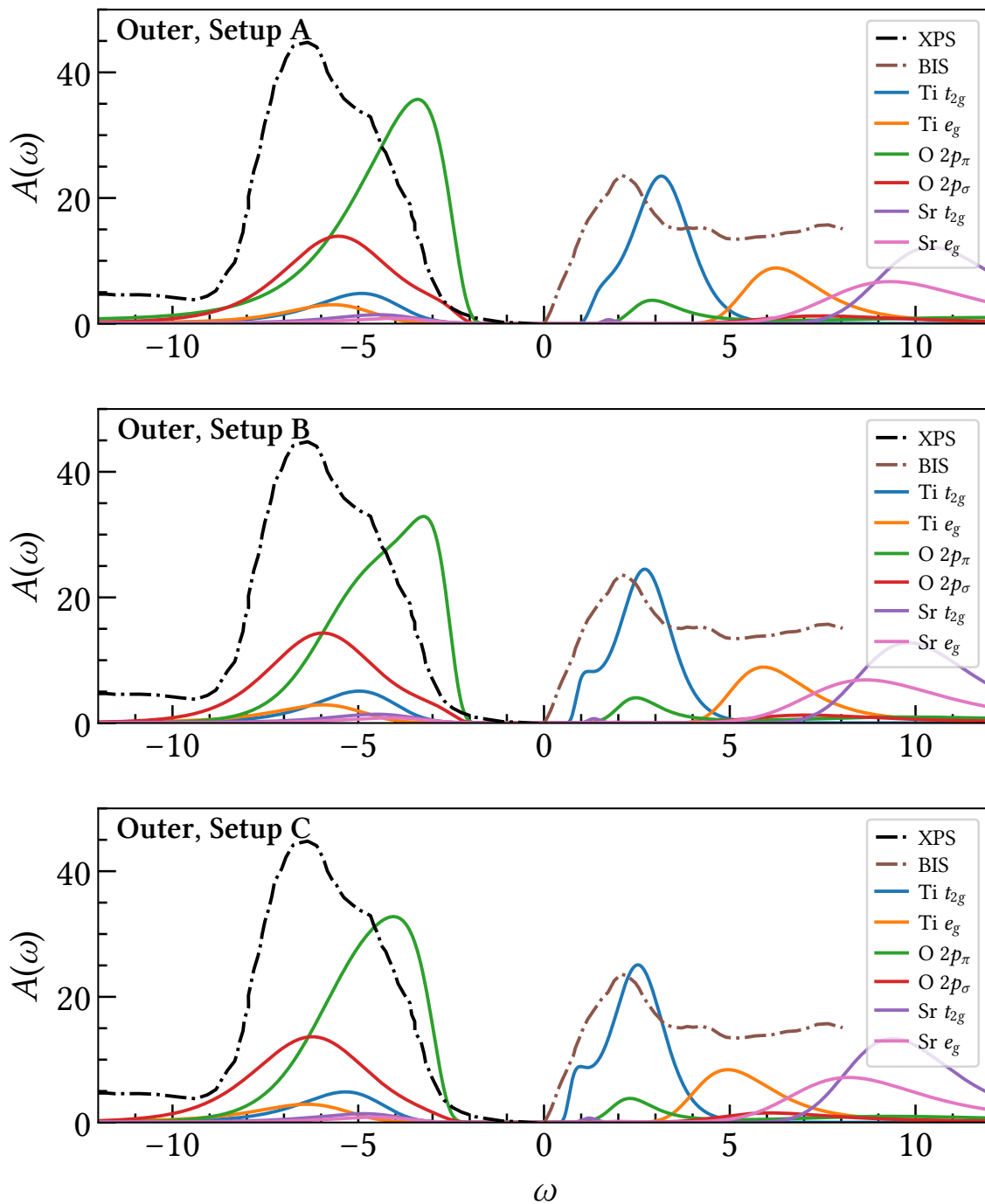
Figure 3.6: SEET outer-loop local orbitally resolved spectral functions for setup A (Ti t_{2g}), B (Ti t_{2g}; O p_π; O p_σ), C (Ti t_{2g}; Ti e_g; O p_π; O p_σ). Experimental XPS and IPES data from Ref. [54, 55].
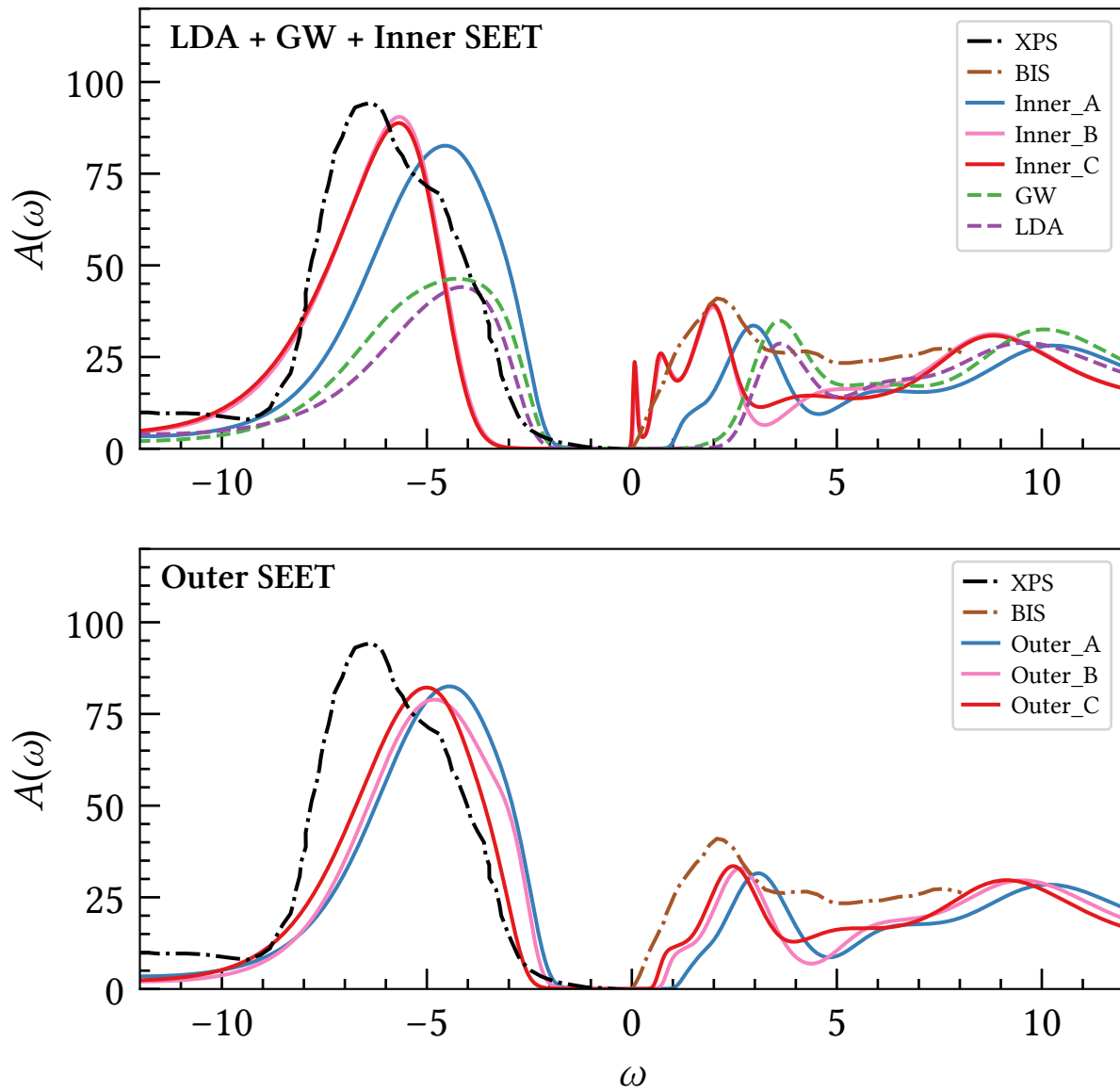
Figure 3.7: Local total spectra comparison. Experimental XPS and IPES data from Ref. [54, 55].

Appendix A

Schur Algorithm Code

Program Title: Nevanlinna
Programming Language: C++
Dependency: Eigen3 and GMP libraries

- Prepare a file for input parameters. Our example needs the file name of the Matsubara Green's function data (ifile), the number of Matsubara points (imag_num) and where to output spectral function (ofile).
- Prepare the Matsubara Green's function data file (in the format of 'frequency real_part imag_part\n' with increasing positive Matsubara frequencies)
- Change the real grid descretization as needed, including the minimum and maximum frequency, number of discretized points and eta *i.e.* η (evaluation axis is $\omega + i\eta$) in Listing A.5 line number 74.
- Change output from $A(\omega)$ to $G^R = -\mathcal{N}\mathcal{G}(\omega + i\eta)$ or else as needed in Listing A.5 line number 95.
- Change calculation precision in Listing A.3 line number 10 as needed. A typical sufficient precision for Schur algorithm is 128.
- Can output the ultimate $\{a(z), b(z), c(z), d(z)\}$ in Listing A.4 line number 92 for convenience of calculating the functional norm during optimization, without the need to rerun this program.
- This program can also be used to evaluate $A(\omega)$ with an optimized θ_{M+1}. Change the constant 0 θ_{M+1} in Listing A.4 line number 90 to the formula for your $\theta_{M+1}(z)$.
- Compile the program with gnu c++ compiler and run the executable ./nevanlinna with input redirection.

Listing A.1: compile and run the program

```
1  g++ -o nevanlinna nevanlinna.cpp -I path/to/eigen3 -lgmp -lgmpxx
2  ./nevanlinna < input.txt
```

Listing A.2: input.txt

```
1  ifile imag_num ofile
```

Listing A.3: nevanlinna.cpp

```
1  #include "schur.h"
2
3
4  int main (int argc, char * argv[]) {
5      std::string ifile, ofile, coefile;
6      int imag_num;
7      //prompt user for input parameters
8      std::cin >> ifile >> imag_num >> ofile >> coefile;
9      //set calculation precision
```

```cpp
10      mpf_set_default_prec(1024);
11      //begin evaluation
12      Schur<mpf_class> NG(ifile, imag_num, ofile);
13      NG.evaluation(coefile);
14      return 0;
15  }
```

Listing A.4: schur.h

```cpp
1  #include "nevanlinna.h"
2
3
4  //convert number to string with n precision
5  template <typename T>
6  std::string to_string_p(const T a_value, const int n = 80){
7      std::ostringstream out;
8      out.precision(n);
9      out << std::fixed << a_value;
10      return out.str();
11  }
12
13
14  template <class T>
15  class Schur : precision_<T> {
16  private:
17      using typename precision_<T>::nev_complex;
18      using typename precision_<T>::nev_complex_vector;
19      using typename precision_<T>::nev_complex_matrix;
20      using typename precision_<T>::nev_complex_matrix_vector;
21  public:
22      //check Nevanlinna/contractive interpolant existence condition
23      Schur (std::string ifile, int imag_num, std::string ofile);
24      //evaluation with 0 parametric function
25      void evaluation (std::string cofile);
26  private:
27      int M; //number of Matsubara points
28      imag_domain_data <T> imag; //theta values at Matsubara points (G -> NG ->
             theta)
29      real_domain_data <T> real; //real frequency NG storage, at omega + i*eta
30      nev_complex_vector phis; //phi_1 to phi_M
31      nev_complex_matrix_vector abcds; //intermediate {a, b, c, d}s used to
             calculate phis
32      //memoize intermediate abcds and calculate phis by iteration
33      void core ();
34  };
35
36
37  template <class T>
38  Schur<T>::Schur (std::string ifile, int imag_num, std::string ofile) : imag(ifile,
        imag_num), real(ofile)  {
39      M = imag_num;
40      //fill the Pick matrix
41      nev_complex_matrix Pick (M, M);
42      nev_complex I {0., 1.};
43      for (int i = 0; i < M; i++) {
44          for (int j = 0; j < M; j++) {
45              nev_complex freq_i = (imag.freq()[i] - I) / (imag.freq()[i] + I);
46              nev_complex freq_j = (imag.freq()[j] - I) / (imag.freq()[j] + I);
```

```cpp
47                 nev_complex one {1., 0.};
48                 nev_complex nom = one - imag.val()[i] * std::conj(imag.val()[j]);
49                 nev_complex den = one - freq_i * std::conj(freq_j);
50                 Pick(i, j) = nom / den;
51             }
52         }
53         //check the positive semi-definiteness of the Pick matrix using Cholesky
               decomposition
54         Eigen::LLT<nev_complex_matrix> lltOfPick(Pick + nev_complex_matrix::Identity(M
               , M) * 1e-250);
55         if(lltOfPick.info() == Eigen::NumericalIssue)
56             std::cerr << "Pick matrix is non positive semi-definite matrix in Schur
                   method." << std::endl;
57         else std::cerr << "Pick matrix is positive semi-definite." << std::endl;
58  }
59
60
61  template <class T>
62  void Schur<T>::core() {
63      phis.resize(M);
64      abcds.resize(M);
65      phis[0] = imag.val()[0];
66      for (int k = 0; k < M; k++) abcds[k] = nev_complex_matrix::Identity(2, 2);
67      for (int j = 0; j < M - 1; j++) {
68          for (int k = j; k < M; k++) {
69              nev_complex_matrix prod(2, 2);
70              prod(0, 0) = (imag.freq()[k] - imag.freq()[j]) / (imag.freq()[k] - std
                   ::conj(imag.freq()[j]));
71              prod(0, 1) = phis[j];
72              prod(1, 0) = std::conj(phis[j])*
73                          ((imag.freq()[k] - imag.freq()[j]) / (imag.freq()[k] - std
                           ::conj(imag.freq()[j])));
74              prod(1, 1) = nev_complex{1., 0.};
75              abcds[k] *= prod;
76          }
77          phis[j + 1] = (- abcds[j + 1](1, 1) * imag.val()[j + 1] + abcds[j + 1](0,
               1)) /
78                          (abcds[j + 1](1, 0) * imag.val()[j + 1] - abcds[j + 1](0,
                           0));
79      }
80  }
81
82
83  template <class T>
84  void Schur<T>::evaluation (std::string cofile) {
85      core();
86      nev_complex I {0., 1.};
87      nev_complex One {1., 0.};
88      std::ofstream coefile (cofile); //"cofile" ofstream
89      for (int i = 0; i < real.N_real(); i++) {
90          nev_complex_matrix result = nev_complex_matrix::Identity(2, 2);
91          nev_complex z = real.freq()[i];
92          for (int j = 0; j < M; j++) {
93              nev_complex_matrix prod(2, 2);
94              prod(0, 0) = (z - imag.freq()[j]) / (z - std::conj(imag.freq()[j]));
95              prod(0, 1) = phis[j];
96              prod(1, 0) = std::conj(phis[j])*
97                          ((z - imag.freq()[j]) / (z - std::conj(imag.freq()[j])));
```

```
 98              prod(1, 1) = nev_complex{1., 0.};
 99              result *= prod;
100          }
101          nev_complex param {0., 0.}; //theta_{M+1}, choose to be constant function
                 0 here
102          nev_complex theta = (result(0, 0) * param + result(0, 1)) / (result(1, 0)
                 * param + result(1, 1));
103          //output "real.freq(), a.real(), a.imag(), ..., d.imag()\n" into a file
                 for optimization convenience
104          coefile << to_string_p(std::real(real.freq()[i])) << " "
105                  << to_string_p(std::real(result(0, 0))) << " " << to_string_p(std
                         ::imag(result(0, 0))) << " "
106                  << to_string_p(std::real(result(0, 1))) << " " << to_string_p(std
                         ::imag(result(0, 1))) << " "
107                  << to_string_p(std::real(result(1, 0))) << " " << to_string_p(std
                         ::imag(result(1, 0))) << " "
108                  << to_string_p(std::real(result(1, 1))) << " " << to_string_p(std
                         ::imag(result(1, 1))) << std::endl;
109          real.val()[i] = I * (One + theta) / (One - theta); //inverse Mobius
                 transform from theta to NG
110      }
111      real.write();
112 }
```

Listing A.5: nevanlinna.h

```
 1 #include <iostream>
 2 #include <iomanip>
 3 #include <complex>
 4 #include <vector>
 5 #include <fstream>
 6 #include <gmpxx.h>
 7 #include <cmath>
 8 #include <algorithm>
 9 #include <Eigen/Dense>
10
11
12 //precision class is used to define typenames
13 //template T can be any precision type, e.g. double or mpf_class
14 template <class T>
15 class precision_ {
16 protected:
17     using nev_real = T;
18     using nev_complex = std::complex<T>;
19     using nev_complex_vector = std::vector<nev_complex>;
20     using nev_complex_matrix = Eigen::Matrix<nev_complex, Eigen::Dynamic, Eigen::
         Dynamic>;
21     using nev_complex_matrix_vector = std::vector<nev_complex_matrix>;
22 };
23
24
25 //Matsubara data storage (theta values)
26 template <class T>
27 class imag_domain_data : precision_<T> {
28 private:
29     using typename precision_<T>::nev_real;
30     using typename precision_<T>::nev_complex;
31     using typename precision_<T>::nev_complex_vector;
```

```cpp
32  public:
33      //calculate theta (G -> NG -> theta) and store Matsubara frequencies and theta
34      imag_domain_data (std::string ifile, int imag_num) : N_imag_(imag_num) {
35          std::ifstream ifs(ifile);
36          val_.resize(N_imag_);
37          freq_.resize(N_imag_);
38          nev_real freq, re, im;
39          nev_complex I {0., 1.};
40          for (int i = 0; i < N_imag_; i++) {
41              ifs >> freq >> re >> im;
42              nev_complex val = nev_complex{-re, -im}; //minus signs to transform G
                     to NG
43              freq_[i] = nev_complex{0., freq};
44              val_[i] = (val - I) / (val + I); //Mobius transform from NG to theta
45          }
46          //reverse input frequency order (decreasing then) and the corresponding
                 thetas,
47          //which tests to be the most robust interpolation order with Schur
                 algorithm
48          //std::reverse(freq_.begin(),freq_.end());
49          //std::reverse(val_.begin(), val_.end());
50      }
51      //number of Matsubara points
52      int N_imag() const { return N_imag_; }
53      //contractive interpolant theta values at Matsubara points
54      const nev_complex_vector &val() const { return val_; }
55      //Matsubra frequencies
56      const nev_complex_vector &freq() const { return freq_; }
57  private:
58      int N_imag_;
59      nev_complex_vector val_;
60      nev_complex_vector freq_;
61  };
62
63
64  //real frequency NG storage, at omega+i*eta
65  template <class T>
66  class real_domain_data : precision_<T> {
67  private:
68      using typename precision_<T>::nev_real;
69      using typename precision_<T>::nev_complex;
70      using typename precision_<T>::nev_complex_vector;
71  public:
72      //calculate and store real frequencies (at omega+i*eta), uniform grid
73      //***change N_real_, omega_min, omega_max and eta as needed***
74      real_domain_data (std::string ofile) : ofs(ofile), N_real_(6000), omega_min
             (-15), omega_max(0), eta(0.01) {
75          val_.resize(N_real_);
76          freq_.resize(N_real_);
77          nev_real inter = (omega_max - omega_min) / (N_real_ - 1);
78          nev_real temp = omega_min;
79          freq_[0] = nev_complex{omega_min, eta};
80          for (int i = 1; i < N_real_; i++) {
81              temp += inter;
82              freq_[i] = nev_complex{temp, eta};
83          }
84      }
85      //number of real frequencies
```

```cpp
 86        int N_real() const { return N_real_; }
 87        //NG values at real frequencies
 88        nev_complex_vector &val() { return val_; }
 89        //real frequencies
 90        const nev_complex_vector &freq() const { return freq_; }
 91        //write real frequencies and spectral function A(omega) values to the output
                file
 92        void write () {
 93            for(int i = 0;i < N_real_; i++){
 94                ofs << std::fixed << std::setprecision(15);
 95                ofs << freq_[i].real() << " " << 1 / M_PI * val_[i].imag() <<std::endl
                    ;
 96            }
 97        }
 98 private:
 99        std::ofstream ofs;
100        int N_real_;
101        nev_real omega_min;
102        nev_real omega_max;
103        nev_real eta;
104        nev_complex_vector val_;
105        nev_complex_vector freq_;
106 };
```

Bibliography

[1] Robert J. Deltete and Reed A. Guy. "Emerging from Imaginary Time". In: *Synthese* 108.2 (1996), pp. 185–203. ISSN: 00397857, 15730964. URL: http://www.jstor.org/stable/20117541.

[2] Rolf Nevanlinna. *Über beschränkte Funktionen die in gegebenen Punkten vorgeschriebene werte annehmen*. Helsingfors: [Sana], 1919.

[3] J. Schur. "Über Potenzreihen, die im Innern des Einheits-kreises beschränkt sind". In: *Journal für die reine und angewandte Mathematik (Crelles Journal)* 1918 (148 1918), pp. 122 –145. DOI: 10.1515/crll.1918.148.122. URL: https://www-degruyter-com.proxy.lib.umich.edu/view/journals/crll/1918/148/article-p122.xml.

[4] Vadym M. Adamyan and Igor M Tkachenko. "Reconstruction of Distributions by Their Moments and Local Constraints". In: *North-Holland Mathematics Studies* 189 (2001), pp. 321 –333. DOI: 10.1016/S0304-0208(01)80057-8. URL: https://www-sciencedirect-com.proxy.lib.umich.edu/science/article/pii/S0304020801800578?via%3Dihub.

[5] Georg Pick. "Über die Beschränkungen analytischer Funktionen, welche durch vorgegebene Funktionswerte bewirkt werdenber die Beschränkungen analytischer Funktionen, welche durch vorgegebene Funktionswerte bewirkt werden". In: *Mathematische annalen* 78 (1 - 4 1917), pp. 270 –275. DOI: 10.1007/BF01457103. URL: https://link.springer.com/article/10.1007/BF01456817.

[6] P Khargonekar and A Tannenbaum. "Non-Euclidian metrics and the robust stabilization of systems with parameter uncertainty". In: *IEEE Transactions on Automatic Control* 30 (10 1917), pp. 1005 –1013. DOI: 10.1109/TAC.1985.1103805. URL: https://ieeexplore-ieee-org.proxy.lib.umich.edu/document/1103805.

[7] N.I. Akhiezer. *The Classical Moment Problem and Some Related Questions in Analysis*. London: Oliver and Boyd., 1965.

[8] Emanuel Gull. "Continuous-Time Quantum Monte Carlo Algorithms for Fermions". PhD thesis. 2008, p. 161.

[9] Gong-ning Chen. "The General Rational Interpolation Problem and Its Connection with the Nevanlinna-Pick Interpolation and Power Moment Problem". In: *Linear Algebra and its Application* 273 (1 1998), pp. 83 –117. DOI: 10.1016/S0024-3795(97)00346-7. URL: https://www.sciencedirect.com/science/article/pii/S0024379597003467?via%3Dihub.

[10] Miroslav Fiedler. "Quasidirect Decompositions of Hankel and Toeplitz Matrices". In: *Applied Mathematics Research eXpress* 2003 (2 2003), pp. 33 –70. DOI: 10.1155/S1687120003212028. URL: https://academic.oup.com/amrx/article/2003/2/33/212288.

[11] Herbert Amann, Hanspeter Kraft, and Marvin Rosenblum. *Topics in Hardy Classes and Univalent Functions*. Birkhäuser Boston, 1994.

[12] Brian M. Adams et al. *Dakota, a multilevel parallel object-oriented framework for design optimization, parameter estimation, uncertainty quantification, and sensitivity analysis*. May 2014. DOI: 10.2172/1177077.

[13] Hiroshi Shinaoka et al. "Compressing Green's function using intermediate representation between imaginary-time and real-frequency domains". In: *Phys. Rev. B* 96 (3 2017), p. 035147. DOI: 10.1103/PhysRevB.96.035147. URL: https://link.aps.org/doi/10.1103/PhysRevB.96.035147.

[14] Jia Li et al. "Sparse sampling approach to efficient ab initio calculations at finite temperature". In: *Phys. Rev. B* 101 (3 2020), p. 035144. DOI: 10.1103/PhysRevB.101.035144. URL: https://link.aps.org/doi/10.1103/PhysRevB.101.035144.

[15] R. Blankenbecler, D. J. Scalapino, and R. L. Sugar. "Monte Carlo calculations of coupled boson-fermion systems. I". In: *Phys. Rev. D* 24 (8 1981), pp. 2278–2286. DOI: 10.1103/PhysRevD.24.2278. URL: https://link.aps.org/doi/10.1103/PhysRevD.24.2278.

[16] Emanuel Gull et al. "Continuous-time Monte Carlo methods for quantum impurity models". In: *Rev. Mod. Phys.* 83 (2 2011), pp. 349–404. DOI: 10.1103/RevModPhys.83.349. URL: https://link.aps.org/doi/10.1103/RevModPhys.83.349.

[17] Joost VandeVondele and Jürg Hutter. "Gaussian basis sets for accurate calculations on molecular systems in gas and condensed phases". In: *The Journal of Chemical Physics* 127.11 (2007), p. 114105. DOI: 10.1063/1.2770708. eprint: https://doi.org/10.1063/1.2770708. URL: https://doi.org/10.1063/1.2770708.

[18] S. Goedecker, M. Teter, and J. Hutter. "Separable dual-space Gaussian pseudopotentials". In: *Phys. Rev. B* 54 (3 1996), pp. 1703–1710. DOI: 10.1103/PhysRevB.54.1703. URL: https://link.aps.org/doi/10.1103/PhysRevB.54.1703.

[19] Chia-Nan Yeh et al. *Electron correlations in cubic paramagnetic perovskite Sr(V,Mn)O$_3$ from fully self-consistent self-energy embedding theory*. in preparation.

[20] Lars Hedin. "New Method for Calculating the One-Particle Green's Function with Application to the Electron-Gas Problem". In: *Phys. Rev.* 139 (3A 1965), A796–A823. DOI: 10.1103/PhysRev.139.A796. URL: https://link.aps.org/doi/10.1103/PhysRev.139.A796.

[21] Ryan Levy, J.P.F. LeBlanc, and Emanuel Gull. "Implementation of the maximum entropy method for analytic continuation". In: *Computer Physics Communications* 215 (2017), pp. 149 –155. ISSN: 0010-4655. DOI: https://doi.org/10.1016/j.cpc.2017.01.018. URL: http://www.sciencedirect.com/science/article/pii/S0010465517300309.

[22] K. Yoshimatsu et al. "Dimensional-Crossover-Driven Metal-Insulator Transition in SrVO$_3$ Ultrathin Films". In: *Phys. Rev. Lett.* 104 (14 2010), p. 147601. DOI: 10.1103/PhysRevLett.104.147601. URL: https://link.aps.org/doi/10.1103/PhysRevLett.104.147601.

[23] K. Morikawa et al. "Spectral weight transfer and mass renormalization in Mott-Hubbard systems SrVO$_3$ and CaVO$_3$: Influence of long-range Coulomb interaction". In: *Phys. Rev. B* 52 (19 1995), pp. 13711–13714. DOI: 10.1103/PhysRevB.52.13711. URL: https://link.aps.org/doi/10.1103/PhysRevB.52.13711.

[24] Christof Hättig. "Optimization of auxiliary basis sets for RI-MP2 and RI-CC2 calculations: Core–valence and quintuple-ζ basis sets for H to Ar and QZVPP basis sets for Li to Kr". In: *Phys. Chem. Chem. Phys.* 7 (1 2005), pp. 59–66. DOI: 10.1039/B415208E. URL: http://dx.doi.org/10.1039/B415208E.

[25] Ph. Delsarte, Y. Genin, and Y. Kamp. "The Nevanlinna-Pick Problem for Matrix-Valued Functions". In: *SIAM Journal on Applied Mathematics* 36.1 (1979), pp. 47–61. ISSN: 00361399. URL: http://www.jstor.org/stable/2100767.

[26] Guanrong Chen and Çetin Kaya Koç. "Computing matrix-valued Nevanlinna-Pick interpolation". In: *Linear Algebra and its Applications* 203-204 (1994), pp. 253 –263. ISSN: 0024-3795. DOI: https://doi.org/10.1016/0024-3795(94)90205-4. URL: http://www.sciencedirect.com/science/article/pii/0024379594902054.

[27] Karsten Balzer and Martin Eckstein. "Auxiliary Hamiltonian representation of the nonequilibrium Dyson equation". In: *Phys. Rev. B* 89 (3 2014), p. 035148. DOI: 10.1103/PhysRevB.89.035148. URL: https://link.aps.org/doi/10.1103/PhysRevB.89.035148.

[28] Christian Gramsch and Michael Potthoff. "Lehmann representation of the nonequilibrium self-energy". In: *Phys. Rev. B* 92 (23 2015), p. 235135. DOI: 10.1103/PhysRevB.92.235135. URL: https://link.aps.org/doi/10.1103/PhysRevB.92.235135.

[29] Christian Gramsch et al. "Hamiltonian-based impurity solver for nonequilibrium dynamical mean-field theory". In: *Phys. Rev. B* 88 (23 2013), p. 235106. DOI: 10.1103/PhysRevB.88.235106. URL: https://link.aps.org/doi/10.1103/PhysRevB.88.235106.

[30] Tudor D. Stanescu and Gabriel Kotliar. "Fermi arcs and hidden zeros of the Green function in the pseudogap state". In: *Phys. Rev. B* 74 (12 2006), p. 125110. DOI: 10.1103/PhysRevB.74.125110. URL: https://link.aps.org/doi/10.1103/PhysRevB.74.125110.

[31] Shiro Sakai et al. "Cluster-size dependence in cellular dynamical mean-field theory". In: *Phys. Rev. B* 85 (3 2012), p. 035102. DOI: 10.1103/PhysRevB.85.035102. URL: https://link.aps.org/doi/10.1103/PhysRevB.85.035102.

[32] Cuneyt Yazici and Hulya Kodal Sevindir. "A correction for computing matrix-valued Nevanlinna-Pick interpolation problem". In: *AIP Conference Proceedings* 1558.1 (2013), pp. 2474–2477. DOI: 10.1063/1.4826042. eprint: https://aip.scitation.org/doi/pdf/10.1063/1.4826042. URL: https://aip.scitation.org/doi/abs/10.1063/1.4826042.

[33] A. F. Santander-Syro et al. "Two-dimensional electron gas with universal subbands at the surface of SrTiO3". In: *Nature* 469.7329 (2011), pp. 189–193. ISSN: 1476-4687. DOI: 10.1038/nature09720. URL: https://doi.org/10.1038/nature09720.

[34] T. F. Nova et al. "Metastable ferroelectricity in optically strained SrTiO3". In: *Science* 364.6445 (2019), pp. 1075–1079. ISSN: 0036-8075. DOI: 10.1126/science.aaw4911. eprint: https://science.sciencemag.org/content/364/6445/1075.full.pdf. URL: https://science.sciencemag.org/content/364/6445/1075.

[35] M. Itoh et al. "Ferroelectricity Induced by Oxygen Isotope Exchange in Strontium Titanate Perovskite". In: *Phys. Rev. Lett.* 82 (17 1999), pp. 3540–3543. DOI: 10.1103/PhysRevLett.82.3540. URL: https://link.aps.org/doi/10.1103/PhysRevLett.82.3540.

[36] P. A. Fleury, J. F. Scott, and J. M. Worlock. "Soft Phonon Modes and the 110°K Phase Transition in $SrTiO_3$". In: *Phys. Rev. Lett.* 21 (1 1968), pp. 16–19. DOI: 10.1103/PhysRevLett.21.16. URL: https://link.aps.org/doi/10.1103/PhysRevLett.21.16.

[37] Darrell G. Schlom et al. "Strain Tuning of Ferroelectric Thin Films". In: *Annual Review of Materials Research* 37.1 (2007), pp. 589–626. DOI: 10.1146/annurev.matsci.37.061206.113016. eprint: https://doi.org/10.1146/annurev.matsci.37.061206.113016. URL: https://doi.org/10.1146/annurev.matsci.37.061206.113016.

[38]   Hiromoto Uwe and Tunetaro Sakudo. "Stress-induced ferroelectricity and soft phonon modes in SrTiO$_3$". In: *Phys. Rev. B* 13 (1 1976), pp. 271–286. DOI: 10.1103/PhysRevB.13.271. URL: https://link.aps.org/doi/10.1103/PhysRevB.13.271.

[39]   Qing-Yan Wang et al. "Interface-Induced High-Temperature Superconductivity in Single Unit-Cell *FeSe* Films on *SrTiO$_3$*". In: *Chinese Physics Letters* 29.3 (2012), p. 037402. DOI: 10.1088/0256-307x/29/3/037402. URL: https://doi.org/10.1088%2F0256-307x%2F29%2F3%2F037402.

[40]   Jian-Feng Ge et al. "Superconductivity above 100 K in single-layer FeSe films on doped SrTiO3". In: *Nature Materials* 14.3 (2015), pp. 285–289. ISSN: 1476-4660. DOI: 10.1038/nmat4153. URL: https://doi.org/10.1038/nmat4153.

[41]   Kui-juan Jin et al. "Positive colossal magnetoresistance from interface effect in $p-n$ junction of La$_{0.9}$Sr$_{0.1}$MnO$_3$ and SrNb$_{0.01}$Ti$_{0.99}$O$_3$". In: *Phys. Rev. B* 71 (18 2005), p. 184428. DOI: 10.1103/PhysRevB.71.184428. URL: https://link.aps.org/doi/10.1103/PhysRevB.71.184428.

[42]   Marianne C. Tarun, Farida A. Selim, and Matthew D. McCluskey. "Persistent Photoconductivity in Strontium Titanate". In: *Phys. Rev. Lett.* 111 (18 2013), p. 187403. DOI: 10.1103/PhysRevLett.111.187403. URL: https://link.aps.org/doi/10.1103/PhysRevLett.111.187403.

[43]   K. van Benthem, C. Elsässer, and R. H. French. "Bulk electronic structure of SrTiO3: Experiment and theory". In: *Journal of Applied Physics* 90.12 (2001), pp. 6156–6164. DOI: 10.1063/1.1415766. eprint: https://doi.org/10.1063/1.1415766. URL: https://doi.org/10.1063/1.1415766.

[44]   Lorenzo Sponza et al. "Role of localized electrons in electron-hole interaction: The case of SrTiO$_3$". In: *Phys. Rev. B* 87 (23 2013), p. 235102. DOI: 10.1103/PhysRevB.87.235102. URL: https://link.aps.org/doi/10.1103/PhysRevB.87.235102.

[45]   Giancarlo Cappellini et al. "Structural properties and quasiparticle energies of cubic SrO, MgO and SrTiO3". In: *Journal of Physics: Condensed Matter* 12.15 (2000), pp. 3671–3688. DOI: 10.1088/0953-8984/12/15/315. URL: https://doi.org/10.1088%2F0953-8984%2F12%2F15%2F315.

[46]   Sergei Iskakov et al. "Ab initio self-energy embedding for the photoemission spectra of NiO and MnO". In: *Physical Review B* 102.8 (2020). ISSN: 2469-9969. DOI: 10.1103/physrevb.102.085105. URL: http://dx.doi.org/10.1103/PhysRevB.102.085105.

[47]   Qiming Sun et al. "PySCF: the Python-based simulations of chemistry framework". In: *WIREs Computational Molecular Science* 8.1 (2018), e1340. DOI: https://doi.org/10.1002/wcms.1340. eprint: https://onlinelibrary.wiley.com/doi/pdf/10.1002/wcms.1340. URL: https://onlinelibrary.wiley.com/doi/abs/10.1002/wcms.1340.

[48]   Alicia Rae Welden, Alexander A. Rusakov, and Dominika Zgid. "Exploring connections between statistical mechanics and Green's functions for realistic systems: Temperature dependent electronic entropy and internal energy from a self-consistent second-order Green's function". In: *The Journal of Chemical Physics* 145.20 (2016), p. 204106. DOI: 10.1063/1.4967449. eprint: https://doi.org/10.1063/1.4967449. URL: https://doi.org/10.1063/1.4967449.

[49] Sergei Iskakov et al. "Effect of propagator renormalization on the band gap of insulating solids". In: *Physical Review B* 100.8 (2019). ISSN: 2469-9969. DOI: 10.1103/physrevb.100.085112. URL: http://dx.doi.org/10.1103/PhysRevB.100.085112.

[50] Takao Kotani, Mark van Schilfgaarde, and Sergey V. Faleev. "Quasiparticle self-consistent *GW* method: A basis for the independent-particle approximation". In: *Phys. Rev. B* 76 (16 2007), p. 165106. DOI: 10.1103/PhysRevB.76.165106. URL: https://link.aps.org/doi/10.1103/PhysRevB.76.165106.

[51] Chia-Nan Yeh. *GW approximation for solids with density fitting note*. 2019.

[52] B. Reihl et al. "Electronic structure of strontium titanate". In: *Phys. Rev. B* 30 (2 1984), pp. 803–806. DOI: 10.1103/PhysRevB.30.803. URL: https://link.aps.org/doi/10.1103/PhysRevB.30.803.

[53] T. Higuchi et al. "Electronic structure of *p*-type SrTiO$_3$ by photoemission spectroscopy". In: *Phys. Rev. B* 57 (12 1998), pp. 6978–6983. DOI: 10.1103/PhysRevB.57.6978. URL: https://link.aps.org/doi/10.1103/PhysRevB.57.6978.

[54] Daisuke Baba et al. "Unoccupied Electronic State of Lightly La-Doped SrTiO3Observed by Inverse-Photoemission Spectroscopy". In: *Japanese Journal of Applied Physics* 42.Part 2, No. 7B (2003), pp. L837–L839. DOI: 10.1143/jjap.42.l837. URL: https://doi.org/10.1143%2Fjjap.42.l837.

[55] Yasuhisa Tezuka et al. "Photoemission and Bremsstrahlung Isochromat Spectroscopy Studies of TiO2 (Rutile) and SrTiO3". In: *Journal of the Physical Society of Japan* 63.1 (1994), pp. 347–357. DOI: 10.1143/JPSJ.63.347. eprint: https://doi.org/10.1143/JPSJ.63.347. URL: https://doi.org/10.1143/JPSJ.63.347.